

Pareto-Optimal Domino-Tiling of Orthogonal Polygon Phased Arrays

P. Rocca,⁽¹⁾⁽²⁾ *Senior Member, IEEE*, N. Anselmi,⁽¹⁾ *Member, IEEE*, A. Polo,⁽¹⁾ *Member, IEEE*,
and A. Massa,⁽¹⁾⁽³⁾⁽⁴⁾ *Fellow, IEEE*

⁽¹⁾ *CNIT* - "University of Trento" Research Unit

Via Sommarive 9, 38123 Trento - Italy

E-mail: {*nicola.anselmi, paolo.rocca, andrea.massa*}@unitn.it

Website: www.eledia.org/eledia-unitn

⁽²⁾ *ELEDIA Research Center (ELEDIA@XIDIAN* - Xidian University)

P.O. Box 191, No.2 South Tabai Road, 710071 Xi'an, Shaanxi Province - China

E-mail: *paolo.rocca@xidian.edu.cn*

Website: www.eledia.org/eledia-xidian

⁽³⁾ *ELEDIA Research Center (ELEDIA@UESTC* - UESTC)

School of Electronic Engineering, Chengdu 611731 - China

E-mail: *andrea.massa@uestc.edu.cn*

Website: www.eledia.org/eledia-uestc

⁽⁴⁾ *ELEDIA Research Center (ELEDIA@TSINGHUA* - Tsinghua University)

30 Shuangqing Rd, 100084 Haidian, Beijing - China

E-mail: *andrea.massa@tsinghua.edu.cn*

Website: www.eledia.org/eledia-tsinghua

This work has been submitted to the IEEE for possible publication. Copyright may be transferred without notice, after which this version may no longer be accessible.

Pareto-Optimal Domino-Tiling of Orthogonal Polygon Phased Arrays

P. Rocca, N. Anselmi, A. Polo, and A. Massa

Abstract

The modular design of planar phased arrays arranged on orthogonal polygon-shaped apertures is addressed and a new method is proposed to synthesize domino-tiled arrays fitting multiple, generally conflicting, requirements. Starting from an analytic procedure to check the domino-tileability of the aperture, two multi-objective optimization techniques are derived to efficiently and effectively deal with small and medium/large arrays depending on the values of the bounds for the cardinality of the solution space of the admissible clustered solutions. A set of representative numerical examples is reported to assess the effectiveness of the proposed synthesis approach also through full-wave simulations when considering non-ideal models for the radiating elements of the array.

Key words: Phased Array Antenna, Planar Array, Orthogonal Polygon-Shaped Apertures, Irregular Tiling, Domino Tiles, Multi-Objective Optimization.

1 Introduction

Modern wireless applications need antenna systems with fast scanning capabilities, accurate beam pointing, interference rejection, and multiple beams. Phased arrays (*PA*s) fit these requirements [1]-[3] being able to simultaneously accomplish different and complex tasks in a reliable manner as well as to quickly adapt to the surrounding environment. Therefore, they represent a key-enabling technology for developing a variety of civil applications like 5G communications [4]-[6], autonomous driving [7]-[9], next generation weather and air traffic control radar systems [10]-[12] just to mention a few. Accordingly, *PA*s are currently deployed in cars, drones, and 5G handsets with severe constraints on the antenna aperture, which is usually irregular, due to the limited space and the integration with other co-located electronic devices (e.g., microchips and micro-controllers that are usually used to implement high levels of digitization). On the other hand, classical *PA* design techniques are mainly concerned with regular apertures with rectangular, square, or circular shapes. Consequently, the development of efficient and reliable *ad-hoc* methods for synthesizing *PA*s arranged on irregular regions is strongly suggested to fully exploit the available area and to guarantee the synthesis of optimal trade-offs between radiation performance, complexity, and costs. In the last years, several unconventional architectures have been proposed and suitable *PA* design methodologies have been implemented (see [13] and the reference therein) to yield cost-effective and high-performance antenna array solutions [14]. In such a framework, sub-arrayed arrangements of the array elements have attracted a non-negligible attention thanks to their capabilities to fit challenging radiation requirements by implementing high-performance radiating systems with affordable costs. Indeed, sub-arrayed *PA*s implement the antenna functionalities at the sub-array level by reducing the number of radio-frequency chains and transmit-received modules (*TRMs*) with respect to classical/fully-populated arrays having complete beam-forming networks. Irregular clustering methods, which use either sub-arrays of arbitrary shapes and/or sizes [15]-[21] or tiles with pre-defined shapes and sizes [22]-[26], have been widely studied. Such techniques define an irregular organization of the array clusters in the antenna aperture, which results in an aperiodic distribution of the sub-array phase centers, to reduce the presence and the level of undesired quantization lobes that severely affect the performance of *PA*s when the beam scanning and the operation bandwidth

increase [3]. Recently, the synthesis of irregular tiled arrays that cover the antenna aperture to maximize the antenna efficiency and its directivity, subject to the antenna size, has been addressed with enumerative [27][28] and analytic-driven optimization-based [29]-[31] strategies. Theorems on the tileability of the array aperture with simple tile shapes, such as dominoes [29], diamonds [31], or two-sizes squares [30], have been stated and successfully exploited to derive effective uniform clustering methods. However, they are limited to regular apertures (e.g., rectangular [29][30] and hexagonal [31]) and tile shapes (e.g., dominoes [29], diamonds [31], and squares [30]).

This work faces with the first limitation of current tiling methods by proposing a novel method for designing domino-tiled planar *PAs* arranged on arbitrary orthogonal polygon apertures. First, the *height function*, which has been introduced in [32] for efficiently coding a domino-based array arrangement, is here exploited to derive the condition on the tileability of the antenna aperture by recurring to a proper application of the theorems in [33][34]. It is worth pointing out the relevance of this result for modern wireless systems where there are hard limitations on the antenna dimensions and thus the need of guaranteeing the maximum aperture efficiency. Furthermore, starting from the approach in [29], a new design method based on two multi-objective optimization techniques is here proposed to synthesize domino-tiled configurations of planar *PAs* with arbitrary orthogonal polygon apertures fitting multiple conflicting antenna requirements [35]-[37].

The paper is organized as follows. Section 2 describes the formulation of the tiling synthesis problem at hand and the corresponding tileability theorems. Two versions of a multi-objective design method are then presented in Sect. 3, while Section 4 is devoted to a numerical validation of the proposed synthesis approach along with a performance assessment. Eventually, some conclusions are drawn (Sect. 5).

2 Mathematical Formulation

Let us consider a planar (2D) PA with P elements, each one belonging to a square unit cell (i.e., a *pixel*)⁽¹⁾. The ensemble of the P unit cells defines a simply-connected region⁽²⁾ in the $x - y$ plane so that the array aperture \mathcal{O} turns out to be an orthogonal polygon defined as a polygon where every edge of the contour is either horizontal (i.e., along the x direction) or vertical (i.e., along the y direction) [38]. Moreover, the inter-element spacing between the centers of two adjacent pixel cells along the x -axis and the y -axis is equal to d_x (x -axis) and d_y (y -axis) [Fig. 1(a)], respectively, while the maximum number of unit cells along the same orthogonal directions is N and M [Fig. 1(b)]. The array elements are clustered in Q ($Q \triangleq \frac{P}{2}$) elementary “bricks”, $\sigma = \{\sigma_q; q = 1, \dots, Q\}$, which are denoted as *tiles*, having domino shapes and grouping two neighbouring pixels sharing one side (Fig. 1). Since the manufacturing of a single tile is doable only if the EM field generated by the p -th ($p = 1, \dots, P$) elementary radiator, $E_p(\theta, \phi)$, is invariant with respect to a 90 [deg] rotation with respect to the z -axis, two types of dominoes are used. More specifically, the tile shapes are a vertical domino, $\sigma_q = \sigma^V$, and a horizontal one, $\sigma_q = \sigma^H$, that combine two adjacent pixels sharing a horizontal or a vertical edge, respectively. Each q -th ($q = 1, \dots, Q$) tile is controlled by an amplifier and a phase shifter to weight in amplitude, α_q , and/or phase, β_q , the received/transmitted signal at the sub-array level [Fig. 1(a)].

The far-field pattern radiated by the array is then given by

$$P(\theta, \phi) = \left| \sum_{q=1}^Q \alpha_q \left\{ \sum_{p=1}^P \delta_{c_{pq}} E_p(\theta, \phi) e^{j \frac{2\pi}{\lambda} (x_p \sin \theta \cos \phi + y_p \sin \theta \sin \phi)} \right\} e^{j \beta_q} \right|^2 \quad (1)$$

where $E_p(\theta, \phi)$ is the *embedded/active-element pattern* [2][3] of the p -th ($p = 1, \dots, P$) array element, λ is the wavelength, (θ, ϕ) are the angular coordinates, (x_p, y_p) are the Cartesian coordinates of the center of the p -th ($p = 1, \dots, P$) unit cell of the array, while $\delta_{c_{pq}}$ is the

⁽¹⁾For the sake of notation simplicity, each pixel is hereinafter supposed to include only one radiating element. However, it is worth noticing that this is not an hypothesis for the proposed tiling method since each “cell” is a logical unit and, physically, it can include one or more radiating elements without any loss of generality of the underlying theoretical formulation.

⁽²⁾A simply-connected region is a domain in which any simple closed curve can continuously shrink into a point while remaining in the same domain. As for the 2D case, a simply-connected domain is an area without holes.

Kronecker delta function ($\delta_{c_p q} = 1$ if $c_p = q$ or $\delta_{c_p q} = 0$ when $c_p \neq q$), c_p being the integer index ($c_p \in [1, Q]$) whose value indicates the membership of the p -th ($p = 1, \dots, P$) array element to the q -th ($q = 1, \dots, Q$) tile [Fig. 1(b)]. Moreover, let us define the vectors $\boldsymbol{\alpha} = \{\alpha_q; q = 1, \dots, Q\}$, $\boldsymbol{\beta} = \{\beta_q; q = 1, \dots, Q\}$, and $\mathbf{c} = \{c_p; p = 1, \dots, P\}$ for notation simplicity. Accordingly, the array tiling problem addressed in this work can be formulated as follows:

Array Tiling Synthesis - Given an array of $M \times N$ elements displaced on an antenna aperture \mathcal{O} with orthogonal polygon shape, find the optimal clustering of the array elements, \mathbf{c}^{opt} (i.e., a complete tessellation of \mathcal{O}), by using Q domino tiles and the corresponding sub-array amplitudes, $\boldsymbol{\alpha}^{opt}$, and phases, $\boldsymbol{\beta}^{opt}$, such that the radiated power pattern $P^{opt}(\theta, \phi)$ fits a set of K user-defined requirements.

To address such a *Synthesis Problem*, an innovative design strategy is proposed (Sect. 3) that makes use of an analytic procedure to check the domino-tileability of the aperture \mathcal{O} as well as to derive useful bounds on the cardinality of the solution space of the admissible clustering configurations. Those latter items are detailed in the following.

2.1 Tileability Theorem and Cardinality Bounds

Given an orthogonal polygon-shaped aperture \mathcal{O} , the analytic procedure for *a-priori* determining whether the aperture is fully domino-tileable is based on the *height function*, which has been firstly introduced in [32] and then used in [39] to develop an efficient algorithm for the exhaustive generation of all the domino-tiles configurations completely covering a surface. Such an approach has been exploited in [29] for the domino-tiling of rectangular arrays, but here it is non-trivially extended and generalized to more complex and arbitrary orthogonal polygon antenna apertures.

Towards this end, let us consider the set of the vertices of the P unit cells of the aperture \mathcal{O} , $\mathbf{v} = \{v_g; g = 1, \dots, G\}$, [Fig. 2(a)] composed by boundary, $\mathbf{b} = \{b_s; s = 1, \dots, S\}$ ($b_s \in \partial\mathcal{O}$, $\partial\mathcal{O}$ being the boundary of \mathcal{O}), and internal, $\mathbf{a} = \{a_l; l = 1, \dots, L\}$ ($a_l \notin \partial\mathcal{O}$), elements [Fig. 2(b)] so that $\mathbf{v} = \mathbf{b} \cup \mathbf{a}$. Moreover, a chessboard pattern for the P pixels in \mathcal{O} is considered [Fig. 2(c)] and the notation $v_g \rightarrow v_e$ ($v_g \leftarrow v_e$) is used to indicate an edge oriented from v_g towards v_e (vice-versa) and connecting the two adjacent vertices v_g and v_e of the set \mathbf{v} [Fig. 2(c)].

The value of the height function, ψ , for the boundary vertices ($\boldsymbol{\psi} \triangleq \{\psi(b_s); s = 1, \dots, S\}$) is then computed by setting $\psi(b_1) = 0$ [Fig. 2(c)] and applying the following rule

$$\psi(b_s) = \begin{cases} \psi(b_{s-1}) + 1 & \text{if } (b_{s-1} \rightarrow b_s) \\ \psi(b_{s-1}) - 1 & \text{if } (b_{s-1} \leftarrow b_s) \end{cases} \quad (2)$$

for the remaining external entries ($s > 1$).

Furthermore, the boundary set \boldsymbol{b} is also described by the corresponding S values of the *auxiliary function* χ [33], $\{\chi(b_s); s = 1, \dots, S\}$, being

$$\chi(b_s) = \min_{b_g \in \partial\mathcal{O}} [\gamma(b_g, b_s)] \quad (3)$$

where $\gamma(b_g, b_s) \triangleq \psi(b_g) + \Delta(b_g, b_s)$ and $\Delta(b_g, b_s)$ is the number of edges of the shortest path from the boundary edge b_g to the other one b_s through the graph \mathcal{G} [Fig. 2(c)], \mathcal{G} being a directed graph built by connecting the neighboring elements of the vertices set \boldsymbol{v} and with edges that are oriented clockwise/counter-clockwise if they belong to a white/black pixel [Fig. 2(c)].

The array aperture \mathcal{O} turns out to be fully domino-tileable if the following condition (*Orthogonal-Polygon Tileability*) holds true [33]:

$$\psi(b_s) = \chi(b_s), \quad s = 1, \dots, S. \quad (4)$$

For instance, the array aperture \mathcal{O} in Fig. 2(c) fulfils (4) as pictorially shown in Fig. 1, while the one in Fig. 3 does not comply the tileability condition even though it has an equal number of white and black pixels. As a representative example, let us check (4) for the border vertex b_8 . Since the element of \boldsymbol{b} that provides the minimum value of γ is the boundary vertex $v_5 = b_{17}$, it turns out that $\chi(b_8) = 1$ being $\psi(b_{17}) = -2$ and $\Delta(b_{17}, b_8) = 3$. Differently, $\psi(b_8) = 5$ and therefore the region \mathcal{O} of Fig. 3 is not fully-tileable with dominoes.

Of course, the tileability condition is a pre-requisite for starting the design of an irregular sub-arrayed *PA* with a user-defined tile shape, but certainly an estimate of the dimension of the solution space of the admissible set of complete tiled arrangements is very important, as well. Indeed, the “knowledge” of the number T of existing domino tilings is a key-stone for defin-

ing/choosing the most suitable synthesis strategy to determine the optimal solution fitting the *PA* requirements. Unlike rectangular apertures [29][40], there is no closed-form relation for T when dealing with arbitrary apertures, but it is still possible to estimate the problem cardinality by defining an upper, T_u , and a lower, T_l , bound of the number of domino arrangements that fully cover the aperture \mathcal{O} .

The upper bound value, T_u , is equal to the number of tiling configurations fully covering the smallest regular $M \times N$ rectangle including the orthogonal polygon \mathcal{O} [29], $\tau(M, N)$, which depends on the array dimensions, M and N , as follows

$$\tau(M, N) = 2^{\frac{MN}{2}} \prod_{m=1}^M \prod_{n=1}^N \left[\cos^2 \left(\frac{\pi m}{M+1} \right) + \cos^2 \left(\frac{\pi n}{N+1} \right) \right]^{1/4}, \quad (5)$$

while the lower bound, T_l , is given by

$$T_l = \sum_{j=1}^J \tau(M_j, N_j) \quad (6)$$

M_j and N_j ($j = 1, \dots, J$) being the dimensions of J disjoint rectangles covering \mathcal{O} [Fig. 4(a)]. To give a pictorial indication on the dimension of the solution space of the tiling problem at hand, the behaviour of the T bounds for the orthogonal polygon shape in Fig. 4(a) when setting $N = 12$ and varying M within the range $6 \leq M \leq 30$ is shown in Fig. 4(b).

3 Orthogonal Polygon Array Design Methods

The array tiling problem formulated in Sect. 2 is intrinsically a multi-objective synthesis problem (*MOP*) where K , generally conflicting, requirements have to be satisfied. Mathematically, “the solution” of such a *MOP* turns out to be a Pareto-front (*PF*) of optimal (i.e., *non-dominated*) trade-off solutions [41] fitting the design specifications coded into K cost function terms, $\Phi_k(\mathbf{c}, \boldsymbol{\alpha}, \boldsymbol{\beta})$, $k = 1, \dots, K$. Towards this end, a synthesis strategy, which is based on two multi-objective optimization techniques, for the tiling of orthogonal polygon arrays is here presented.

3.1 EPF Method (EPFM)

Once checked the *Orthogonal Polygon Tileability condition* to guarantee the tileability of the aperture \mathcal{O} , the first tiling method allows one to fully determine the *PF* of the trade-off solutions when the synthesis problem at hand is computationally affordable (i.e., the *CPU*-time for processing at most T_u admissible domino arrangements is reasonable/moderate) thanks to an exhaustive generation of all (T) possible tiling configurations. More in detail, the *Exact PF Method (EPFM)* implements the following procedural steps:

- **Step 0 - Reference Array Definition** - Determine the set of the amplitude, $\alpha^{ref} = \{\alpha_p^{ref}; p = 1, \dots, P\}$, and the phase, $\beta^{ref} = \{\beta_p^{ref}; p = 1, \dots, P\}$, coefficients of a fully-populated array affording a pattern compliant with the design requirements;
- **Step 1 - Tilings Generation** - Starting from the knowledge of the S -size height function vector, ψ , determine the *minimal* tiling $\mathbf{c}^{(1)}$ [29]. Generate the whole set of tilings, \mathbf{C} ($\mathbf{C} \triangleq \{\mathbf{c}^{(t)}; t = 1, \dots, T\}$), by using the Enumerative Tiling Method (*ETM*) [29] to iteratively yield the t -th ($t = 2, \dots, T$) domino arrangement, $\mathbf{c}^{(t)}$, from the previous one, $\mathbf{c}^{(t-1)}$;
- **Step 2 - Excitations Computation** - For each t -th ($t = 1, \dots, T$) tiling configuration compute the sub-array amplitudes, $\alpha^{(t)}$, and phase, $\beta^{(t)}$, weights as follows

$$\begin{pmatrix} \alpha_q^{(t)} \\ \beta_q^{(t)} \end{pmatrix} = \frac{1}{2} \sum_{p=1}^P \begin{pmatrix} \alpha_p^{ref} \\ \beta_p^{ref} \end{pmatrix} \delta_{cpq} \quad (7)$$

($q = 1, \dots, Q$);

- **Step 3 - Tilings Evaluation** - For each t -th ($t = 1, \dots, T$) array clustering, evaluate the K -size cost function vector $\Phi^{(t)}$ ($\Phi^{(t)} \triangleq \{\Phi_k(\mathbf{c}^{(t)}, \alpha^{(t)}, \beta^{(t)}); k = 1, \dots, K\}$);
- **Step 4 - EPF Definition** - For each (t, z)-th ($t, z = 1, \dots, T, z \neq t$) couple of tilings, $(\mathbf{c}^{(t)}, \mathbf{c}^{(z)})$, select the *non-dominated* [35] solution $\mathbf{c}^{(f)}$, that is, $\mathbf{c}^{(f)} = \mathbf{c}^{(t)}$ if ⁽³⁾

⁽³⁾Without loss of generality, the *dominance condition* is here referred to a design problem where all the K cost function terms, $\{\Phi_k(\mathbf{c}^{(t)}); k = 1, \dots, K\}$, have to be minimized.

$$\Phi_k(\mathbf{c}^{(t)}, \boldsymbol{\alpha}^{(t)}, \boldsymbol{\beta}^{(t)}) \leq \Phi_k(\mathbf{c}^{(z)}, \boldsymbol{\alpha}^{(z)}, \boldsymbol{\beta}^{(z)})$$

($k = 1, \dots, K$) and it exists a h -th ($h \in [1, K]$) cost function term such that

$$\Phi_h(\mathbf{c}^{(t)}, \boldsymbol{\alpha}^{(t)}, \boldsymbol{\beta}^{(t)}) < \Phi_h(\mathbf{c}^{(z)}, \boldsymbol{\alpha}^{(z)}, \boldsymbol{\beta}^{(z)}) \quad (8)$$

or $\mathbf{c}^{(f)} = \mathbf{c}^{(z)}$, otherwise;

- **Step 5 - Optimal Tiling Computation** - Starting from the knowledge of the set of F optimal trade-off tilings belonging to the EPF , \mathbf{C}^{PF} ($\mathbf{C}^{PF} \triangleq \{\mathbf{c}^{(f)}; f = 1, \dots, F\}$), choose as \mathbf{c}^{opt} the domino arrangement \mathbf{c}^{MMD} that minimizes the *Minimum Manhattan Distance* (MMD) [35] ($\mathbf{c}^{opt} = \mathbf{c}^{MMD}$)

$$(\mathbf{c}^{MMD}, \boldsymbol{\alpha}^{MMD}, \boldsymbol{\beta}^{MMD}) = \arg \left[\min_{f=1, \dots, F} \{ \|\boldsymbol{\Phi}^{(f)} - \boldsymbol{\Phi}^{(ideal)}\|_1 \} \right] \quad (9)$$

where $\|\cdot\|_1$ stands for the L1 norm, while $\boldsymbol{\Phi}^{(f)}$ ($\boldsymbol{\Phi}^{(f)} \triangleq \{\hat{\Phi}_k^{(f)}; k = 1, \dots, K\}$) and $\boldsymbol{\Phi}^{(ideal)}$ ($\boldsymbol{\Phi}^{(ideal)} \triangleq \{\Phi_k^{(ideal)}; k = 1, \dots, K\}$) are two K -size vectors whose k -th ($k = 1, \dots, K$) elements are

$$\hat{\Phi}_k^{(f)} = \frac{\Phi_k(\mathbf{c}^{(f)}, \boldsymbol{\alpha}^{(f)}, \boldsymbol{\beta}^{(f)})}{\max_{f=1, \dots, F} [\Phi_k(\mathbf{c}^{(f)}, \boldsymbol{\alpha}^{(f)}, \boldsymbol{\beta}^{(f)})] - \min_{f=1, \dots, F} [\Phi_k(\mathbf{c}^{(f)}, \boldsymbol{\alpha}^{(f)}, \boldsymbol{\beta}^{(f)})]}, \quad (10)$$

and

$$\Phi_k^{(ideal)} = \min_{f=1, \dots, F} [\hat{\Phi}_k^{(f)}(\mathbf{c}^{(f)}, \boldsymbol{\alpha}^{(f)}, \boldsymbol{\beta}^{(f)})], \quad (11)$$

respectively.

It is worth pointing out that the *Step 5* is not mandatory, since “the solution” of a *MOP* cannot be, by definition, a single one if the project requirements are conflicting. Indeed, the outcome of a multi-objective optimization is a *PF* of trade-off solutions (*Step 4*) where the designer could freely choose a *PF* element as the optimal one according to the design requirements and the other constraints such as manufacturing issues or costs, which are not involved here in the synthesis process. In this work, *Step 5* has been added to allow an easier and general (i.e., not

subjective and not on a user-needs case-by-case basis) analysis of the outcomes of the proposed tiling method (Sect. 4).

3.2 *APF Method (APFM)*

Whether the exhaustive generation of all T tiling configurations can be executed in an acceptable time (e.g., hours of computations) for small apertures, the evaluation time of multiple cost function terms becomes quickly unfeasible (e.g., years of computations) for larger arrays. Therefore, the second tiling technique, which is denoted as *Approximate PF Method (APFM)*, is aimed at approximating the *PF* and it is suitable for medium/large arrays when the evaluation of the fitness of T_l tiling solutions is unfeasible. In particular, the *APFM* is based on the customization to the tiling problem at hand of a *Multi Objective Evolutionary Algorithm (MOEA)* [35][36] that exploits the *Non-dominated Sorting Genetic Algorithm II (NSGA-II)* [36] for sampling the solution space.

Towards this end, the t -th ($t = 1, \dots, T$) trial tiling (i.e., an *individual* when dealing with global optimization) is univocally represented by a tiling word, $\mathbf{w}^{(t)}$, of L letters ($\mathbf{w}^{(t)} \triangleq \{w_l^{(t)}; l = 1, \dots, L\}$), the l -th one being a function of the values of the height function at the internal vertices of \mathcal{O} , \mathbf{a} , given by [29]

$$w_l = \frac{\psi(a_l^{(t)}) - \psi(a_l^{(1)})}{4} \quad (12)$$

where $a_l^{(t)}$ is the l -th ($l = 1, \dots, L$) internal ($a_l^{(t)} \notin \partial\mathcal{O}$) vertex of the t -th tiled array, while $a_l^{(1)}$ refers to the l -th ($l = 1, \dots, L$) vertex of the *minimal tiling* $\mathbf{c}^{(1)}$. Consequently, $\mathbf{w}^{(1)} = \mathbf{0}$ and $0 \leq w_l \leq w_l^{(T)}$, $w_l^{(T)}$ being the l -th ($l = 1, \dots, L$) letter of the T -th tiling word corresponding to the *maximal tiling* $\mathbf{c}^{(T)}$ available in closed-form analogously to $\mathbf{c}^{(1)}$ [29]. Subject to such a word-coding, the *APF* is generated according to the following iterative (i being the iteration index) *NSGA-II*-based procedure:

- **Step 1 - Initialization** ($i = 0$) - Generate the initial alphabet of U words, $\mathcal{P}_i|_{i=0} = \{\mathbf{w}_i^{(u)}|_{i=0}; u = 1, \dots, U\}$ using the schemata-driven initialization in [29] to efficiently sample the solution-space. For each u -th ($u = 1, \dots, U$) word, compute the corresponding

vector $\Phi_i^{(u)} \Big|_{i=0}$ by considering the power pattern $P_i^{(u)}(\theta, \phi) \Big|_{i=0}$ radiated by the corresponding tiling $\mathbf{c}_i^{(u)} \Big|_{i=0}$ and the sub-array amplitudes, $\alpha_i^{(u)} \Big|_{i=0}$, and phases, $\beta_i^{(u)} \Big|_{i=0}$, computed with (7);

- **Step 2 - Pareto Ranking** - Rank the words according to the Pareto dominance criterion (8) defining R -levels PF s [36]. More specifically, the PF of the first level ($r = 1$) is yielded by applying (8) to the whole alphabet \mathcal{P}_i , while the successive r -th ($2 \leq r \leq R$) level PF is derived still using (8), but on a reduced population, $\mathcal{P}_i^{(r)}$, obtained by discarding the words of the previous ($r - 1$)-th PF levels ($\mathcal{P}_i^{(r)} = \mathcal{P}_i^{(r-1)} \cap \left\{ \bigcup_{j=1}^{r-1} \mathcal{P}_i^{(j)} \right\}$). The crowding distance criterion is then used to rank the words within the same r -th ($r = 1, \dots, R$) PF level by increasing the relevance of the corresponding tilings, $\left\{ \mathbf{c}_i^{(u_r)}; u_r = 1, \dots, U_r \right\}$, with higher distance, in the space of the cost functions, with respect to the neighboring ones [36];
- **Step 3 - Alphabet Update** - Update the iteration index ($i \leftarrow i + 1$) and generate a new temporary alphabet \mathcal{Q}_i of U words/individuals by applying the *NSGA-II* generation strategy. Compute the corresponding U -size cost function vector, $\Phi^{(u)}$ ($\Phi^{(u)} \triangleq \{\Phi_i^{(u)}; u = 1, \dots, U\}$). Build a word pool \mathcal{R}_i of $2 \times U$ elements by merging \mathcal{P}_{i-1} and \mathcal{Q}_i ($\mathcal{R}_i = \mathcal{Q}_i \cup \mathcal{P}_{i-1}$), then rank the words of \mathcal{R}_i according to *Step 2* and compose the new alphabet, \mathcal{P}_i , with the first U ranked words;
- **Step 4 - Stopping Criterion** - If the index i is smaller than a user-defined maximum value, I , (i.e., $i < I$), then repeat *Step 2* and *Step 3*. Otherwise, stop the iterative loop and return, as APF , the first ($r = 1$) level PF of the last alphabet, \mathcal{P}_I ;
- **Step 5 - Optimal Tiling Computation** - Eventually, set $\mathbf{c}^{opt} = \mathbf{c}^{MMD}$ (9).

4 Numerical Assessment and Method Validation

The first numerical example refers to the orthogonal polygon array in Fig. 5(a) with $P = 40$ elements distributed on a uniform ($d_x = d_y = \frac{\lambda}{2}$) lattice of $M \times N$ ($M = N = 8$) unit cells. The goal is to synthesize a domino-tiled configuration providing the maximum directivity (D)

and affording a pattern that fulfils the mask $\Pi(u, v)$ in Fig. 5(c). Mathematically, it has been coded by defining the following $K = 2$ cost function terms:

$$\Phi_1(\mathbf{c}, \boldsymbol{\alpha}, \boldsymbol{\beta}) \triangleq \max \left(\frac{4\pi P(u_0, v_0)}{\int_{\Omega} \left[\frac{P(u, v)}{\sqrt{1-u^2-v^2}} \right] du dv} \right) \quad (13)$$

and

$$\begin{aligned} \Phi_2(\mathbf{c}, \boldsymbol{\alpha}, \boldsymbol{\beta}) \triangleq & \min \left(\int_{\Omega} [P(u - u_0, v - v_0) - \Pi(u - u_0, v - v_0)] \right. \\ & \times \mathcal{H}\{P(u - u_0, v - v_0) - \Pi(u - u_0, v - v_0)\} du dv \end{aligned} \quad (14)$$

$\mathcal{H}\{\cdot\}$ and Ω being the Heaviside function and the visible range ($\Omega = \{(u, v) : u^2 + v^2 \leq 1\}$), respectively, while (u_0, v_0) is the beam-pointing direction.

When applying the proposed tiling strategy, the tileability has been firstly checked through (4) once computed the values of the height function at the external-vertices, ψ , [Fig. 5(b)]. As for the cardinality of the solution space, it turns out that $T_u = 12.989 \times 10^6$ and $T_l = 54$. As for the upper bound T_u , it is related to the light-blue square of $M \times N$ pixels in Fig. 5(b) enclosing \mathcal{O} , while the value of T_l is given by the sum of the number of domino tilings of the $J = 4$ rectangles [i.e., the yellow, the magenta, the blue, and the green ones in Fig. 5(b)] within the aperture \mathcal{O} . Since the time for evaluating the two cost function terms (13)-(14) of an array of ideal elements [i.e., $E_p(\theta, \phi) = 1$] is equal to $\Delta t \simeq 0.1$ [sec] on an Intel 2.10GHz Xeon CPU with 64Gb of RAM, the retrieval of the PF would cost at most 15 days wether considering the T_u -wide solution space. However, one can notice that the orthogonal-polygon array in Fig. 5(a) occupies only a limited portion of the $M \times N$ square area. Therefore, the exhaustive ETM -based technique has been applied and the actual number of $T = 9.521 \times 10^3$ configurations has been exhaustively generated and evaluated in $\Delta t_{EPFM} = 16$ [min]. Moreover, the corresponding sub-array weights have been computed through (7) starting from the reference fully-populated excitations, $\boldsymbol{\alpha}^{ref}$, in Fig. 5(a), which have been computed with a convex programming (CP) optimization strategy [42] to fit the power mask constraint displayed in Fig. 5(c). Figure 6 shows the radiated reference power pattern along the principal, $\phi = 0$ [deg] ($v = 0$) and the $\phi = 90$ [deg] ($u = 0$) plane [Fig. 6(b)], while its features are reported in Tab. I. Moreover, Figure 7 plots the PF of the domino-tiled arrays in the (D, SLL) plane along with the representative points of the whole set of admissible tilings. As a representative example, the excitations of

the *MMD* tiling are reported in Fig. 6(a), while Figure 6(b) shows the radiated power pattern with $SLL^{MMD} = -19.62$ [dB] and $D^{MMD} = 19.98$ [dBi], which are close to the values of the same pattern features of the reference solution (Tab. I). For the sake of analysis, the half-power beamwidth in the azimuth ($HPBW_{az}$) and in the elevation ($HPBW_{el}$) planes are given (Tab. I), as well.

The second example deals with the orthogonal polygonal aperture shown in Fig. 8(a) that approximates the circular support of radius $\rho = 2.0\lambda$ with $P = 52$ elements spaced by $d_x = d_y = \frac{\lambda}{2}$. The problem objective is here that of designing a tiled array pointing the beam towards two directions, namely the broadside $(\theta_1, \phi_1) = (0, 0)$ [deg] [i.e., $(u_1, v_1) = (0.0, 0.0)$] and the angle $(\theta_2, \phi_2) = (30, 0)$ [deg] [i.e., $(u_2, v_2) = (0.5, 0.0)$], while fitting the *SLL* requirements stated by the broadside pattern mask in Fig. 8(b) and “translated” for each steering direction (i.e., $SLL^\Pi = -20$ [dB]). According to the mathematical formulation in Sect. 3, this means to define the following $K = 2$ cost functions terms: $\Phi_k(\mathbf{c}, \boldsymbol{\alpha}, \boldsymbol{\beta}) \triangleq \min \left(\int_{\Omega} [P(u - u_k, v - v_k) - \Pi(u - u_k, v - v_k)] \times \mathcal{H} \{ P(u - u_k, v - v_k) - \Pi(u - u_k, v - v_k) \} dudv \right)$, $k = 1, \dots, K$. In order to address the synthesis problem at hand, first the reference fully-populated solution, which is characterized by the set of amplitudes $\boldsymbol{\alpha}^{ref}$ in Fig. 8(a) and radiating the power pattern with $SLL^{ref} = -20.60$ [dB] [Fig. 8(c)], has been obtained with the *CP*. Once the aperture tileability has been verified as well as the possibility to exhaustively sample the solution space of $T_u = 12.989 \times 10^6$ configurations, the *ETM* has been used to generate $T = 2.88 \times 10^4$ different tiles arrangements then evaluated in $\Delta t_{EPFM} = 48$ [min] to retrieve the *PF* shown in Fig. 9. As it can be observed, the *MMD* solution coincides here with the one of the *PF* that better optimizes the $k = 2$ cost function term (*MOP-2* - Fig. 9). The corresponding excitations and patterns are reported in Figs. 10(a)-10(b) and Figs. 10(c)-10(d), respectively. More specifically, it turns out that the *MMD*-tiled array properly steers the beam along the desired directions with a maximum *SLL* degradation, with respect to the ideal reference, of $\Delta_{SLL}^{MMD-ref} \approx 1.5$ [dB] (Tab. II) and a maximum deviation from the target mask of $\Delta_{SLL}^{MMD-\Pi} \approx 0.8$ [dB] [Tab. II - Fig. 11(b)], being $\Delta_{SLL}^{MMD-ref} = \max_k \left| SLL_{(u_k, v_k)}^{MMD} - SLL_{(u_k, v_k)}^{ref} \right|$ and $\Delta_{SLL}^{MMD-\Pi} = \max_k \left| SLL_{(u_k, v_k)}^{MMD} - SLL_{(u_k, v_k)}^\Pi \right|$. For completeness, Figure 11 compares the patterns radiated by the *MMD* array with the reference one and with that generated by the *MOP-1* arrangement

together with the target mask Π when $(u_1, v_1) = (0.0, 0.0)$ [Fig. 11(a) - $v = 0$ plane; Fig. 11(b) - $u = 0$ plane] and $(u_2, v_2) = (0.5, 0.0)$ [Fig. 11(c) - $v = 0$ plane].

Successively, the same test case has been dealt with the *APFM* to assess the reliability and the effectiveness of this latter in approximating the *PF* here available thanks to the *EPFM*. Accordingly, the *MOEA* parameters have been set as follows: $U = L = 37$ (size of the alphabet \mathcal{P}), $I = 100$ (maximum number of iterations), $p_c = 0.9$ (crossover probability), and $p_m = \frac{1}{L}$ (mutation probability)[37]. After $\Delta t_{APFM} = 220$ [sec], the approximate *PF* shown in Fig. 9 (black circles) is derived. As it can be seen, all the *APFM* solutions (black rings - Fig. 9) belong to the *PF* (red dots - Fig. 9) and the success rate is 70%, since 9 among $F = 13$ *PF* solutions have been faithfully recovered, despite the sampling of only 5% (at most) of the whole set of T admissible tilings.

The third example is concerned with a larger elliptically-shaped array [Fig. 12(a)] composed by $P = 224$ elements half-wavelength spaced ($d_x = d_y = \frac{\lambda}{2}$). The synthesis is aimed at fitting the *SLL* mask in Fig. 12(b) when steering the beam at $(\theta_1, \phi_1) = (8, 0)$ [deg] [i.e., $(u_1, v_1) = (0.1392, 0.0)$] and $(\theta_2, \phi_2) = (8, 90)$ [deg] [i.e., $(u_2, v_2) = (0.0, 0.1392)$], thus the same two-terms cost function of the previous example has been considered. Since the aperture shape satisfies the domino tileability condition and, this time, the lower bound is $T_l > 10^{16}$, the *EPFM* is avoided and the *APFM* only is used to determine the solutions *PF*. Starting from the *CP* reference solution in Fig. 12(a), which radiates in broadside the pattern of Fig. 12(c) with $SLL^{ref} = -32.70$ [dB] (Tab. III), the *NSGA-II* loop has been executed by setting the optimization parameters as before ($U = L = 197$, $p_c = 0.9$, $p_m = \frac{1}{L}$) except for the number of iterations, now chosen equal to $I = 1000$, to keep the same percentage of sampling of the solution space due to the wider array size ($P = 224$ vs. $P = 52$). Figure 13 shows the estimated *PF* together with the best *SOP* solution drawn among 10 independent runs of the *GA*-based approach in [29] aimed at optimizing the single-objective cost function given by the linear combination of the two cost function terms, which are independently optimized by the *APFM*. As it can be noticed, several *PF* tilings performs better than the *SOP* one. For instance, the *MMD* solution (Fig. 13) is "described" in Fig. 14. More in detail, the arrangement of the domino tiles is shown in Fig. 14(a) along with the color level representation of the sub-

array amplitudes, while the phase distribution for steering the beam at (u_1, v_1) [Fig. 14(d)] and (u_2, v_2) [Fig. 14(e)] is given in Fig. 14(b) and Fig. 14(c), respectively. As for the radiation performance, it turns out that the maximum degradation of the *SLL* with respect to the reference amounts to $\Delta_{SLL}^{MMD-ref} \approx 2.19$ [dB] (Tab. III) ($\Delta_{SLL}^{MMD-ref} = \Delta_{SLL}^{MMD-\Pi}$), but halving the *TRMs*, while the directivity values are very close ($\Delta_D^{MMD-ref} \approx 0.15$ [dBi] - Tab. III) also thanks to the full coverage of the aperture guaranteed by the proposed synthesis strategy.

The last test case is aimed at investigating the effectiveness of the domino-tiling method in minimizing the beam-pointing error (*BPE*) [43]⁽⁴⁾, due to the quantization of the phase distribution. With reference to the same elliptically-shaped array of Fig. 12(a), the problem at hand is that of fitting the *SLL* mask in Fig. 12(b) and minimizing the *BPE* when scanning the beam within a given cone, $\{\theta_0 \leq \theta \leq \theta_0 + \theta_{max}; 0 \leq \phi \leq 2\pi\}$, θ_{max} being the maximum scan angle. Accordingly, the following cost-function terms have been defined. The former codes the *BPE* requirement, $\Phi_1(\mathbf{c}, \boldsymbol{\alpha}, \boldsymbol{\beta}) \triangleq \min \left\{ \frac{1}{R} \sum_{r=1}^R \xi_r \right\}$, $\xi \triangleq \sqrt{(\theta^{des} - \theta^{act})^2 + (\phi^{des} - \phi^{act})^2}$ and R being the *BPE* and the number of angular directions $\{(\theta_r, \phi_r); r = 1, \dots, R\}$ ($\theta_1 = \theta_0 + \theta_{max}$) that sample the scan range (i.e., $\theta_0 \leq \theta_r \leq \theta_0 + \theta_{max}$ and $0 \leq \phi_r \leq 2\pi$) (Fig. 15), while the other term is related to the *SLL* mask matching

$$\begin{aligned} \Phi_2(\mathbf{c}, \boldsymbol{\alpha}, \boldsymbol{\beta}) \triangleq & \min \left\{ \max_r \left(\int_{\Omega} \left[P(u - [u_0 + u_r^{des}], v - [v_0 + v_r^{des}]) - \right. \right. \right. \\ & \Pi(u - [u_0 + u_r^{des}], v - [v_0 + v_r^{des}]) \times \mathcal{H} \left\{ P(u - [u_0 + u_r^{des}], v - [v_0 + v_r^{des}]) - \right. \\ & \left. \left. \left. \Pi(u - [u_0 + u_r^{des}], v - [v_0 + v_r^{des}]) \right\} dudv \right) \right\} \end{aligned} \quad (15)$$

In particular, three elliptical scan cones with $\theta_{max} = \{30, 45, 60\}$ [deg] from broadside [i.e., $(\theta_0, \phi_0) = (0, 0)$ [deg] $\rightarrow (u_0, v_0) = (0.0, 0.0)$] have been considered and sampled at the $R = 12$ scanning directions reported in Tab. IV. By applying the *APFM*, the *PFs* in Fig. 16 are obtained. With reference to the *MMD* tilings, it turns out that the beam-pointing is kept very accurate (e.g., $\xi_{avg}^{MDD} \big|_{\theta_{max}=30 [deg]} = 0.32$ [deg]) as confirmed by the plots of the *BPE* in Fig. 17 being $\xi^{MDD} \big|_{\theta_{max}=30 [deg]} \leq 1.0$ [deg] [Fig. 17(a)], $\xi^{MDD} \big|_{\theta_{max}=45 [deg]} \leq 1.5$ [deg] [Fig. 17(b)], and $\xi^{MDD} \big|_{\theta_{max}=60 [deg]} \leq 2.7$ [deg] [Fig. 17(c)]. On the contrary, due to the simplicity of the architectural solution (i.e., a tiled array instead of a fully-populated one) and the complexity

⁽⁴⁾The beam-pointing error (*BPE*) is the deviation of the actual beam pointing, $(\theta^{act}, \phi^{act})$, from the desired one, $(\theta^{des}, \phi^{des})$.

of the synthesis problem at hand (i.e., fitting the project requirements on a complete angular cone instead of few steering directions), there is a non-negligible degradation of the *SLL* even though the highest sidelobes do not occur close to the mainbeam as shown in Fig. 18 where the beams generated at four representative scanning directions of Tab. IV (i.e., $\theta_{max} = 30$ [deg] and $r \in \{1, 2, 3, 4\}$) by the *MMD* tiling synthesized when $\theta_{max} = 30$ [deg] are shown.

Finally, the reliability of the proposed tiling strategy and its robustness against the non-idealities of real arrays have been checked. Towards this end, the isotropic elementary radiator of the previous example has been substituted with a rectangular pin-fed patch antenna resonating at $f_0 = 77$ [GHz] and the corresponding element pattern, $E_p(\theta, \phi) \neq 1$ ($p = 1, \dots, P$), has been set to the embedded element pattern of the central element of a neighbour of 5×5 identical elements to include, in the element model, the mutual coupling effects of the real architecture. Despite the difficulty of the synthesis problem at hand, the pattern shape and the beam pointing as well as the relative *SLL* are not significantly altered when introducing a real radiator in the place of the ideal one (Fig. 18), the main differences arising in the far side-lobe region.

5 Conclusions

In this work, the design of orthogonal polygon sub-arrayed arrays with domino tiles has been addressed by means of an innovative design strategy. Starting from the assessment of the full tileability of the polygonal aperture with an analytic procedure, two multi-objective optimization methods have been proposed to synthesize the clustering configuration and the sub-array weights. More specifically, the former method is for compact apertures and it is aimed at determining the Pareto front of the optimal trade-off solutions. The other is suitable for larger arrays and it faithfully approximates the Pareto front.

The key-features of the proposed design strategy are:

- the design of high-efficiency (i.e., full coverage of the aperture without holes) and arbitrary-shaped tiled apertures thanks to the exploitation of suitable mathematical theorems to *a-priori* assess the complete domino-tileability;
- the computationally-effective and reliable retrieval of the Pareto front of optimal trade-off

tilings by means of customized multi-objective methods based on the concept of height function.

Future research activities, beyond the scope of the current work, will be aimed at extending the proposed strategy to different "alphabets" of tiles (i.e., different cardinality and/or tile shapes) of interest for various commercial applications ranging from wireless communications to remote sensing.

Acknowledgements

This work has been partially supported by the Italian Ministry of Education, University, and Research within the Program PRIN 2017 (CUP: E64I19002530001) for the Project CYBER-PHYSICAL ELECTROMAGNETIC VISION: Context-Aware Electromagnetic Sensing and Smart Reaction (EMvisioning) (Grant no. 2017HZJXSZ) and by the Ministry of Education of China within the Chang-Jiang Visiting Professor chair. A. Massa wishes to thank E. Vico for her never-ending inspiration, support, guidance, and help.

References

- [1] R. S. Elliott, *Antenna Theory & Design*. Hoboken, NJ, USA: Wiley IEEE-Press, 2003.
- [2] R. L. Haupt, *Antenna Arrays - A Computation Approach*. Hoboken, NJ, USA: Wiley, 2010.
- [3] R. J. Mailloux, *Phased Array Antenna Handbook*. Boston, MA, USA: Artech House, 2018.
- [4] G. Oliveri, G. Gottardi, F. Robol, A. Polo, L. Poli, M. Salucci, M. Chuan, C. Massagrande, P. Vinetti, M. Mattivi, R. Lombardi, and A. Massa, "Co-design of unconventional array architectures and antenna elements for 5G base stations," *IEEE Trans. Antennas Propag.*, vol. 65, no. 12, pp. 6752-6767, Dec. 2017.
- [5] C. Mao, M. Khalily, P. Xiao, T. W. C. Brown, and S. Gao, "Planar sub-millimeter-wave array antenna with enhanced gain and reduced sidelobes for 5G broadcast applications," *IEEE Trans. Antennas Propag.*, vol. 67, no. 1, pp. 160-168, Jan. 2019.
- [6] J. Zhang, K. Zhao, L. Wang, S. Zhang, and G. F. Pedersen, "Dual-polarized phased array with end-fire radiation for 5G handset applications," *IEEE Trans. Antennas Propag.*, vol. 68, no. 4, pp. 3277-3282, Apr. 2020.
- [7] B. Ku, P. Schmalenberg, O. Inac, O. D. Gurbuz, J. S. Lee, K. Shiozaki, and G. M. Rebeiz, "A 77-81-GHz 16-element phased-array receiver with $\pm 50^\circ$ beam scanning for advanced automotive radars," *IEEE Trans. Microw. Theory Tech.*, vol. 62, no. 11, pp. 2823-2832, Nov. 2014.
- [8] M. Harter, J. Hildebrandt, A. Ziroff, and T. Zwick, "Self-calibration of a 3-D-digital beam-forming radar system for automotive applications with installation behind automotive covers," *IEEE Trans. Microw. Theory Tech.*, vol. 64, no. 9, pp. 2994-3000, Sep. 2016.
- [9] G. F. Hamberger, S. Späth, U. Siart and T. F. Eibert, "A mixed circular/linear dual-polarized phased array concept for automotive radar - Planar antenna designs and system evaluation at 78 GHz," *IEEE Trans. Antennas Propag.*, vol. 67, no. 3, pp. 1562-1572, Mar. 2019.

- [10] J. S. Herd, S. M. Duffy, M. Weber, G. Bringham, C. Weigand, and D. Cursio, "Advanced architecture for a low cost multifunction phased array radar," *Proc. 2010 IEEE MTT-S Int. Microw. Symp.*, Anaheim, CA, USA, pp. 676-679, May 23-28, 2010.
- [11] E. Stailey and K. D. Hondl, "Multifunction phased array radar for aircraft and weather surveillance," *Proc. IEEE*, vol. 104, no. 3, pp. 649-659, Mar. 2016.
- [12] J. D. Díaz, J. L. Salazar-Cerreno, J. A. Ortiz, N. A. Aboserwal, R. M. Lebrón, C. Fulton, and R. D. Palmer, "A cross-stacked radiating antenna with enhanced scanning performance for digital beamforming multifunction phased-array radars," *IEEE Trans. Antennas Propag.*, vol. 66, no. 10, pp. 5258-5267, Oct. 2018.
- [13] P. Rocca, G. Oliveri, R. J. Mailloux, and A. Massa, "Unconventional phased array architectures and design methodologies - A review," *Proc. IEEE*, vol. 104, no. 3, pp. 544-560, Mar. 2016.
- [14] J. S. Herd and M. D. Conway, "The evolution to modern phased array architectures," *Proc. IEEE*, vol. 104, no. 3, pp. 519-529, Mar. 2016.
- [15] P. Lopez, J. A. Rodriguez, F. Ares, and E. Moreno, "Subarray weighting for difference patterns of monopulse antennas: Joint optimization of subarray configurations and weights," *IEEE Trans. Antennas Propag.*, vol. 49, no. 11, pp. 1606-1608, Nov. 2001.
- [16] L. Manica, P. Rocca, A. Martini, and A. Massa, "An innovative approach based on a tree-searching algorithm for the optimal matching of independently optimum sum and difference excitations," *IEEE Trans. Antennas Propag.*, vol. 56, no. 1, pp. 58-66, Jan. 2008.
- [17] L. Manica, P. Rocca, and A. Massa, "Design of subarrayed linear and planar array antennas with SLL control based on an excitation matching approach," *IEEE Trans. Antennas Propag.*, vol. 57, no. 6, pp. 1684-1691, Jun. 2009.
- [18] P. Rocca, L. Manica, R. Azaro, and A. Massa, "A hybrid approach to the synthesis of subarrayed monopulse linear arrays," *IEEE Trans. Antennas Propag.*, vol. 57, no. 1, pp. 280-283, Jan. 2009.

- [19] P. Rocca, L. Manica, and A. Massa, "An improved excitation matching method based on an ant colony optimization for suboptimal-free clustering in sum-difference compromise synthesis," *IEEE Trans. Antennas Propag.*, vol. 57, no. 8, pp. 2297-2306, Aug. 2009.
- [20] X. Yang, W. Xi, Y. Su, T. Zeng, T. Long, and T. K. Sarkar, "Optimization of subarray partition for large planar phased array radar based on weighted K-means clustering method," *IEEE Trans. Antennas Propag.*, vol. 9, no. 8, pp. 1460-1468, Dec. 2015.
- [21] N. Anselmi, P. Rocca, M. Salucci, and A. Massa, "Contiguous phase-clustering in multibeam-on-receive scanning arrays," *IEEE Trans. Antennas Propag.*, vol. 66, no. 11, pp. 5879-5891, Nov. 2018.
- [22] R. J. Mailloux, S. G. Santarelli, T. M. Roberts, and D. Luu, "Irregular polyomino-shaped subarrays for space-based active arrays," *Int. J. Antennas Propag.*, vol. 2009, Article ID 956524, 2009.
- [23] P. Rocca, R. J. Mailloux, and G. Toso, "GA-based optimization of irregular sub-array layouts for wideband phased arrays design," *IEEE Antennas Wireless Propag. Lett.*, vol. 14, pp. 131-134, 2015.
- [24] G. Oliveri, M. Salucci, and A. Massa, "Synthesis of modular contiguously clustered linear arrays through a sparseness-regularized solver," *IEEE Trans. Antennas Propag.*, vol. 64, no. 10, pp. 4277-4287, Oct. 2016.
- [25] B. Avser, J. Pierro, and G. M. Rebeiz, "Random feeding networks for reducing the number of phase shifters in limited-scan arrays," *IEEE Trans. Antennas Propag.*, vol. 64, no. 11, pp. 4648-4658, Nov. 2016.
- [26] Y. Ma, S. Yang, Y. Chen, S. Qu, and J. Hu, "Pattern synthesis of 4-D irregular antenna arrays based on maximum-entropy model," *IEEE Trans. Antennas Propag.*, vol. 67, no. 5, pp. 3048-3057, May 2019.
- [27] Z.-Y. Xiong, Z.-H. Xu, S.-W. Chen, and S.-P. Xiao, "Subarray partition in array antenna based on the algorithm X," *IEEE Antennas Wireless Propag. Lett.*, vol. 12, pp. 906-909, 2013.

- [28] W. Dong, Z. Xu, X. Liu, L. Wang, and S. Xiao, "Modular subarrayed phased-array design by means of iterative convex relaxation optimization," *IEEE Antennas Wirel. Propag. Lett.*, vol. 18, no. 3, pp. 447-451, Mar. 2019.
- [29] N. Anselmi, P. Rocca, and A. Massa, "Irregular phased array tiling by means of analytic schemata-driven optimization," *IEEE Trans. Antennas Propag.*, vol. 65, no. 9, pp. 4495-4510, Sep. 2017.
- [30] P. Rocca, N. Anselmi, A. Polo, and A. Massa, "An irregular two-sizes square tiling method for the design of isophoric phased arrays," *IEEE Trans. Antennas Propag.*, vol. 68, no. 6, pp. 4437-4449, Jun. 2020.
- [31] P. Rocca, N. Anselmi, A. Polo, and A. Massa, "Modular design of hexagonal phased arrays through diamond tiles," *IEEE Trans. Antennas Propag.*, vol. 68, no. 5, pp. 3598-3612, May 2020.
- [32] W. P. Thurston, "Conway's tiling groups," *The American Mathematical Monthly*, vol. 97, no. 8, pp. 757-773, Oct. 1990.
- [33] J-C. Fournier, "Pavage des figures planes sans trous par des dominos: Fondement graphique de l'algorithme de Thurston, parallélisation, unicité et décomposition," *Theor. Comput. Sci.*, vol. 159 no. 1, pp. 105-128, 1996.
- [34] J-C. Fournier, "Tiling pictures of the plane with dominoes," *Discrete Math.*, vol. 165, pp. 313-320, 1997.
- [35] K. Deb, *Multi-Objective Optimization Using Evolutionary Algorithms*. West Sussex, U.K.: Wiley, 2001.
- [36] K. Deb, S. Agrawal, A. Pratap, and T. Meyarivan, "A fast and elitist multi-objective genetic algorithm: NSGA-II," *IEEE Trans. Evol. Comput.*, vol. 6, no. 2, pp. 182-197, Apr. 2002.
- [37] J. Nagar and D. H. Werner, "Multiobjective optimization for electromagnetics and optics: an introduction and tutorial based on real-world applications," *IEEE Antennas Propag. Mag.*, vol. 60, no. 6, pp. 58-71, Dec. 2018.

- [38] Z. Su and R. Ding, “Tiling of orthogonal polygons with similar rectangles and triangles,” *J. Appl. Math. & Computing*, vol. 17, no. 1- 2, pp. 343-350, 2005.
- [39] S. Desreux and E. Remila, “An optimal algorithm to generate tilings,” *J. Discrete Alg.*, no. 4, pp. 168-180, 2006.
- [40] P. Kasteleyn, “The statistics of dimers on a lattice I. The number of dimer arrangements on a quadratic lattice,” *Physica*, vol. 27, pp. 1209-1225, 1961.
- [41] V. Pareto, *Cours d’Economie Politique*. Lausanne: F. Rouge, 1986.
- [42] O. M. Bucci, L. Caccavale, and T. Isernia, “Optimal far-field focusing of uniformly spaced arrays subject to arbitrary upper bounds in nontarget directions,” *IEEE Trans. Antennas Propag.*, vol. 50, no. 11, pp. 1539-1554, Nov. 2002.
- [43] M. I. Skolnik, *Radar Handbook* (3rd Ed.). New York, NY, USA: McGraw-Hill, 2008.

FIGURE CAPTIONS

- **Figure 1.** *Illustrative Example* ($P = 30$) - Sketch of (a) the feeding network of (b) a domino-tiled clustering of an orthogonal polygon shaped aperture with $P = 30$ unit cells.
- **Figure 2.** *Illustrative Example* ($P = 30$) - Sketch of (a) the ordered set of vertices of the P unit cells of \mathcal{O} , $\mathbf{v} = \{v_g; g = 1, \dots, G\}$, consisting of (b) boundary, $\mathbf{b} = \{b_s; s = 1, \dots, S\}$ ($b_s \in \partial\mathcal{O}$), and internal, $\mathbf{a} = \{a_l; l = 1, \dots, L\}$ ($a_l \notin \partial\mathcal{O}$), elements ($\mathbf{v} = \mathbf{b} \cup \mathbf{a}$), and (c) a chessboard pattern for the P pixels in \mathcal{O} along with the corresponding directed graph \mathcal{G} .
- **Figure 3.** *Illustrative Example* ($P = 10, S = 18, L = 2$) - Values of the *height function* at the boundary vertices ($\boldsymbol{\psi} \triangleq \{\psi(b_s); s = 1, \dots, S\}$) along with the shortest path (red arrows) connecting the boundary vertex $v_5 = b_{17}$ to the other one $v_{16} = b_8$ [$\Delta(b_{17}, b_8) = 3$] through the graph \mathcal{G} .
- **Figure 4.** *Illustrative Example* ($N = 12$) - Picture of (a) an orthogonal polygon partitioned into $J = 3$ rectangles and (b) behavior of cardinality bounds when varying M in the range $6 \leq M \leq 30$.
- **Figure 5.** *Numerical Assessment* ($M = 8, N = 8, P = 40, SLL^\Pi = -20$ [dB]) - Plot of (a) the reference fully-populated excitations, $\boldsymbol{\alpha}^{ref}$, (b) the values of the height function at the external vertices, and (c) the power pattern mask, $\Pi(u, v)$.
- **Figure 6.** *Numerical Assessment* ($M = 8, N = 8, P = 40, SLL^\Pi = -20$ [dB]) - Plot of (a) the *MMD* tiling and clusters amplitudes. Plot of (b) the reference and the *MMD* power patterns along the principal, $\phi = 0$ [deg] ($v = 0$) and the $\phi = 90$ [deg] ($u = 0$) planes.
- **Figure 7.** *Numerical Assessment* ($M = 8, N = 8, P = 40, SLL^\Pi = -20$ [dB]) - Plot of the Pareto front of the domino-tiled arrays in the (Φ_1, Φ_2) -plane along with the representative points of the whole set of T admissible tilings.
- **Figure 8.** *Numerical Assessment* ($M = 8, N = 8, P = 52, SLL^\Pi = -20$ [dB]) - Plot of (a) the reference fully-populated excitations, $\boldsymbol{\alpha}^{ref}$, (b) the power pattern mask, $\Pi(u, v)$,

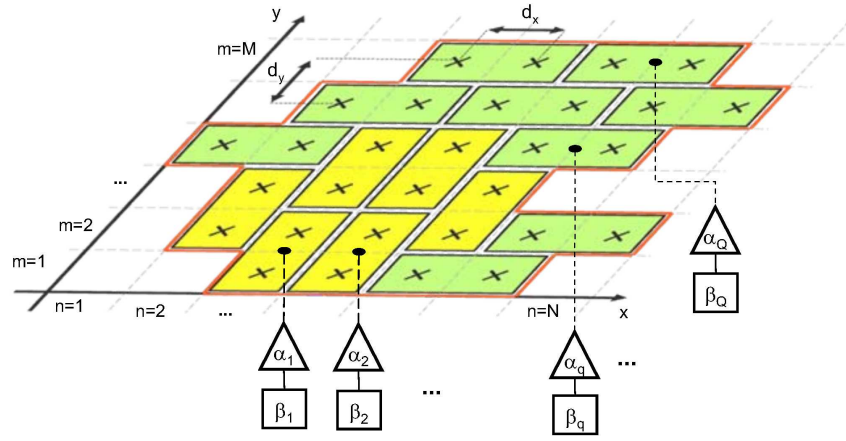
and (c) the reference power pattern.

- **Figure 9.** *Numerical Assessment* ($M = 8, N = 8, P = 52, SLL^\Pi = -20$ [dB]) - Plot of the Pareto front of the domino-tiled arrays in the (Φ_1, Φ_2) -plane along with the representative points of the whole set of T admissible tilings.
- **Figure 10.** *Numerical Assessment* ($M = 8, N = 8, P = 52, SLL^\Pi = -20$ [dB]) - Plot of (a) the amplitude and (b) the phase of the excitations of the *MMD* tiling together with the radiated power patterns at (c) $(u_1, v_1) = (0.0, 0.0)$ and (d) $(u_2, v_2) = (0.5, 0.0)$.
- **Figure 11.** *Numerical Assessment* ($M = 8, N = 8, P = 52, SLL^\Pi = -20$ [dB]) - Plot of the power patterns radiated along (a)(c) the $v = 0$ and (b) the $u = 0$ cuts when pointing the beam at (a)(b) $(u_1, v_1) = (0, 0)$ and (c) $(u_2, v_2) = (0.5, 0)$.
- **Figure 12.** *Numerical Assessment* ($M = 12, N = 26, P = 224, SLL^\Pi = -32.7$ [dB]) - Plot of (a) the reference fully-populated excitations, α^{ref} , (b) the power pattern mask, $\Pi(u, v)$, and (c) the reference power pattern.
- **Figure 13.** *Numerical Assessment* ($M = 12, N = 26, P = 224, SLL^\Pi = -32.7$ [dB]) - Plot of the *APFM* Pareto front of the domino-tiled arrays in the (Φ_1, Φ_2) -plane along with the representative point of the *SOP* optimal arrangement.
- **Figure 14.** *Numerical Assessment* ($M = 12, N = 26, P = 224, SLL^\Pi = -32.7$ [dB]) - Plot of (a) the amplitude and (b)(c) the phase of the excitations of the *MMD* tiling together with the radiated power patterns at (d) $(u_1, v_1) = (0.1392, 0.0)$ and (e) $(u_2, v_2) = (0.0, 0.1392)$.
- **Figure 15.** Sketch of the scan cone, $\{\theta_0 \leq \theta \leq \theta_0 + \theta_{max}; 0 \leq \phi \leq 2\pi\}$, θ_{max} being the maximum scan angle, and of the set of R angular samples, $\{(\theta_r, \phi_r); r = 1, \dots, R\}$ ($\theta_1 = \theta_0 + \theta_{max}$) being $\theta_0 \leq \theta_r \leq \theta_0 + \theta_{max}$ and $0 \leq \phi_r \leq 2\pi$.
- **Figure 16.** *Numerical Assessment* ($M = 12, N = 26, P = 224, SLL^\Pi = -32.7$ [dB]) - Plot of the *APFM* Pareto front of the domino-tiled arrays in the (Φ_1, Φ_2) -plane for different values of the maximum scan angle, $\theta_{max} = \{30, 45, 60\}$ [deg].

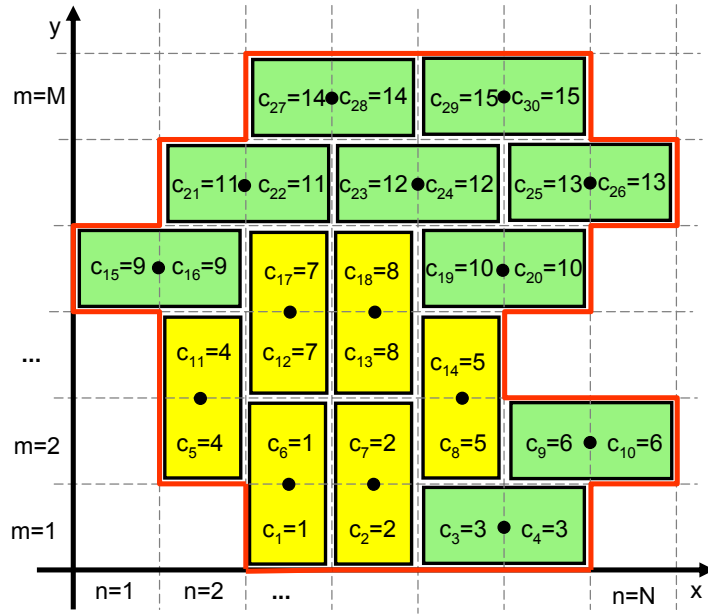
- **Figure 17.** *Numerical Assessment* ($M = 12, N = 26, P = 224, SLL^\Pi = -32.7$ [dB]) - Plot of the *BPE* of the *MMD* domino-tiled array in the scan cone $\{\theta_0 \leq \theta \leq \theta_0 + \theta_{max}; 0 \leq \theta \leq 2\pi\}$ when (a) $\theta_{max} = 30$ [deg], (b) $\theta_{max} = 45$ [deg], and (c) $\theta_{max} = 60$ [deg].
- **Figure 18.** *Numerical Assessment* ($M = 12, N = 26, P = 224, SLL^\Pi = -32.7$ [dB], $\theta_{max} = 30$ [deg]) - Plot of the power patterns radiated by the *MMD* domino-tiled array along the cuts at (a) $\phi = 0$ [deg], (b) $\phi = 16.13$ [deg], (c) $\phi = 40.94$ [deg], and (d) $\phi = 90$ [deg].

TABLE CAPTIONS

- **Table I.** *Numerical Assessment* ($M = 8, N = 8, P = 40, SLL^\Pi = -20$ [dB]) - Pattern features.
- **Table II.** *Numerical Assessment* ($M = 8, N = 8, P = 52, SLL^\Pi = -20$ [dB]) - Pattern features when steering the beam at $(\theta_1, \phi_1) = (0, 0)$ [deg] and $(\theta_2, \phi_2) = (30, 0)$ [deg].
- **Table III.** *Numerical Assessment* ($M = 12, N = 26, P = 224, SLL^\Pi = -32.7$ [dB]) - Pattern features when steering the beam at $(\theta_1, \phi_1) = (8, 0)$ [deg] and $(\theta_2, \phi_2) = (8, 90)$ [deg].
- **Table IV.** List of the angular coordinates of the samples of the scan cone when $\theta_{max} = \{30, 45, 60\}$ [deg].

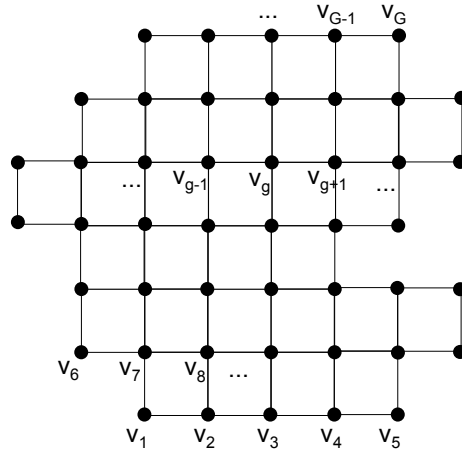


(a)

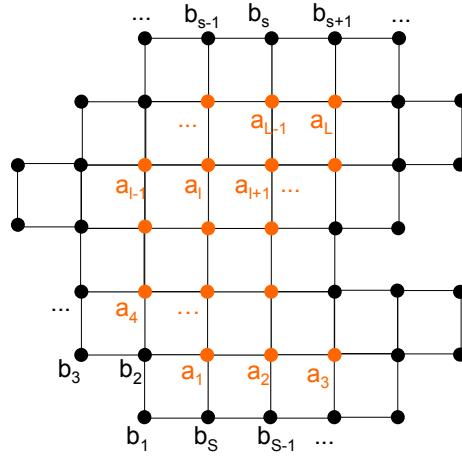


(b)

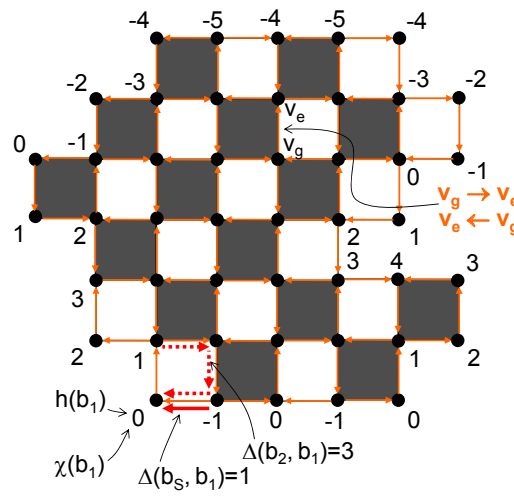
Fig. 1 - P. Rocca et al., “Pareto-Optimal Domino-Tiling of ...”



(a)



(b)



(c)

Fig. 2 - P. Rocca et al., “Pareto-Optimal Domino-Tiling of ...”

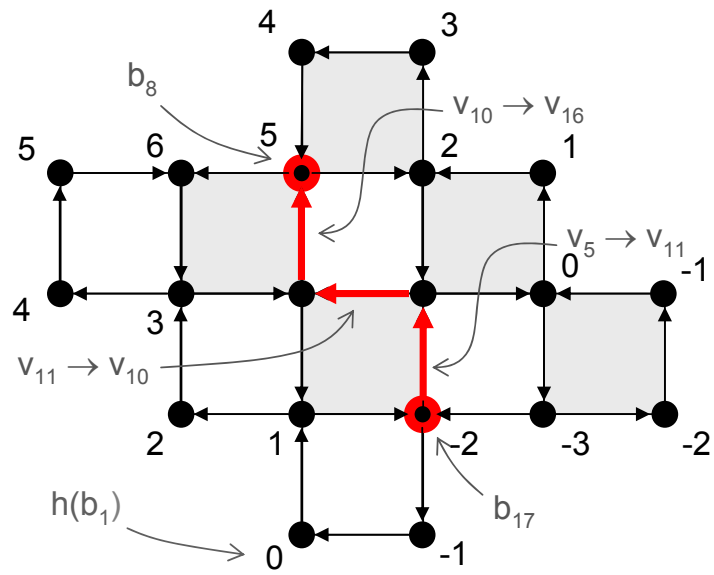


Fig. 3 - P. Rocca et *al.*, “Pareto-Optimal Domino-Tiling of ...”

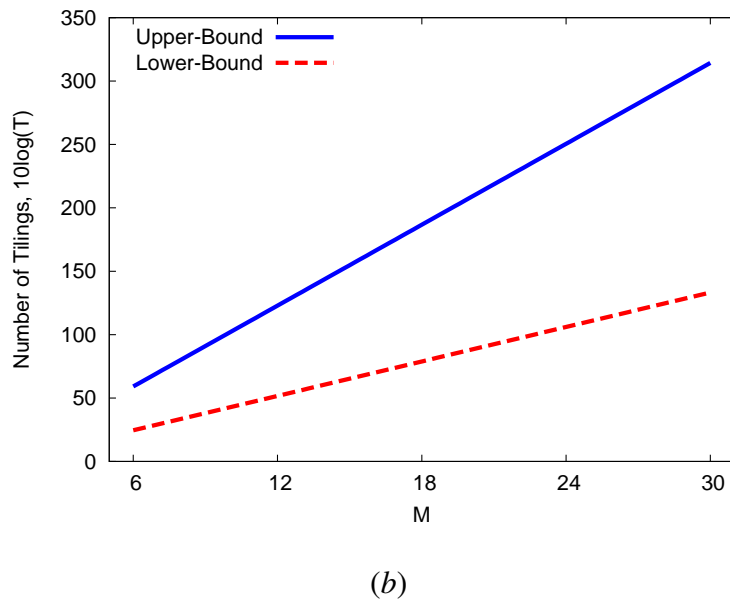
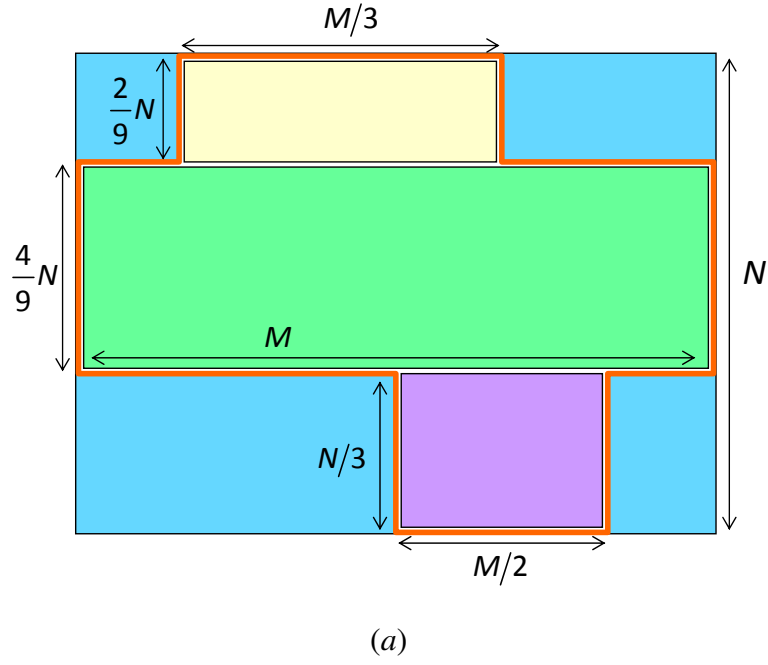
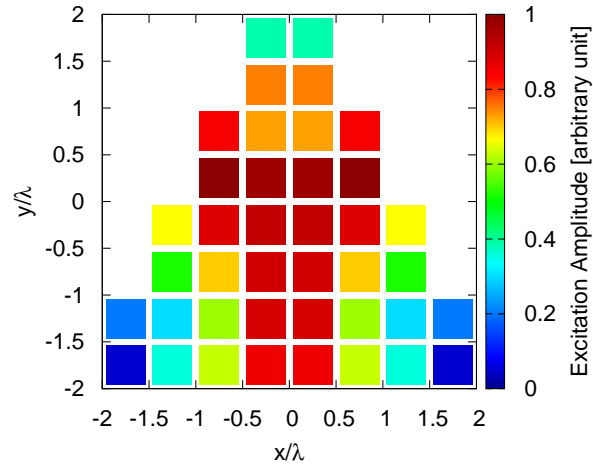
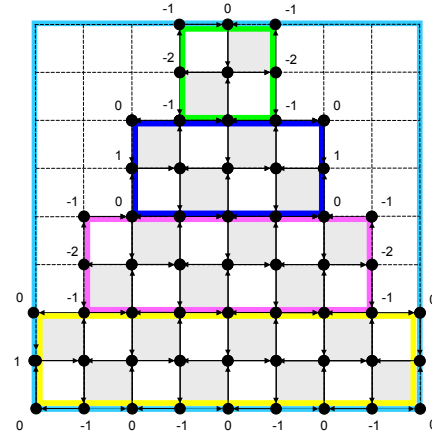


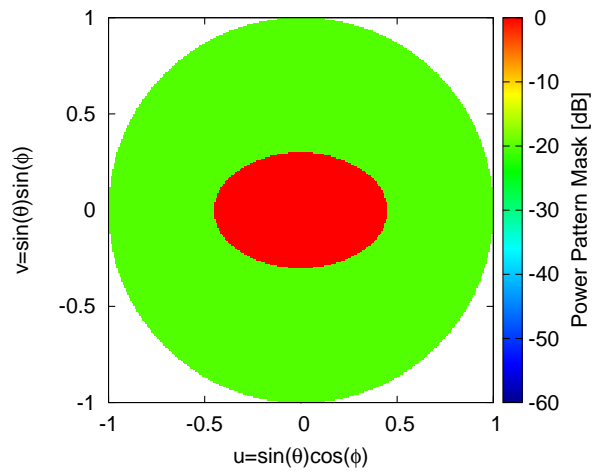
Fig. 4 - P. Rocca et al., “Pareto-Optimal Domino-Tiling of ...”



(a)

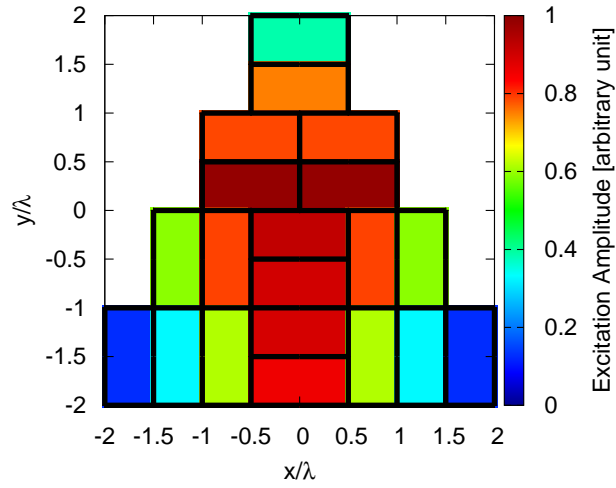


(b)

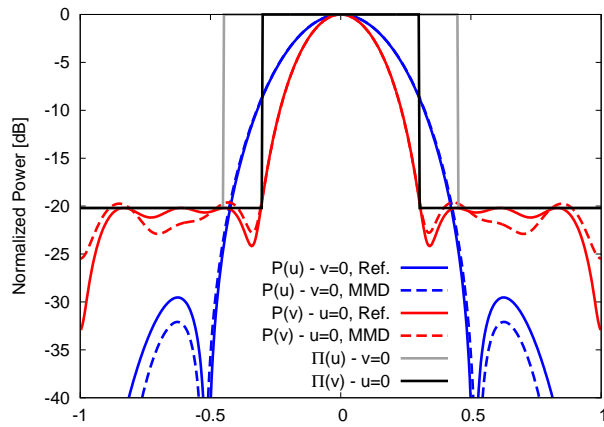


(c)

Fig. 5 - P. Rocca et al., “Pareto-Optimal Domino-Tiling of ...”



(a)



(b)

Fig. 6 - P. Rocca et al., “Pareto-Optimal Domino-Tiling of ...”

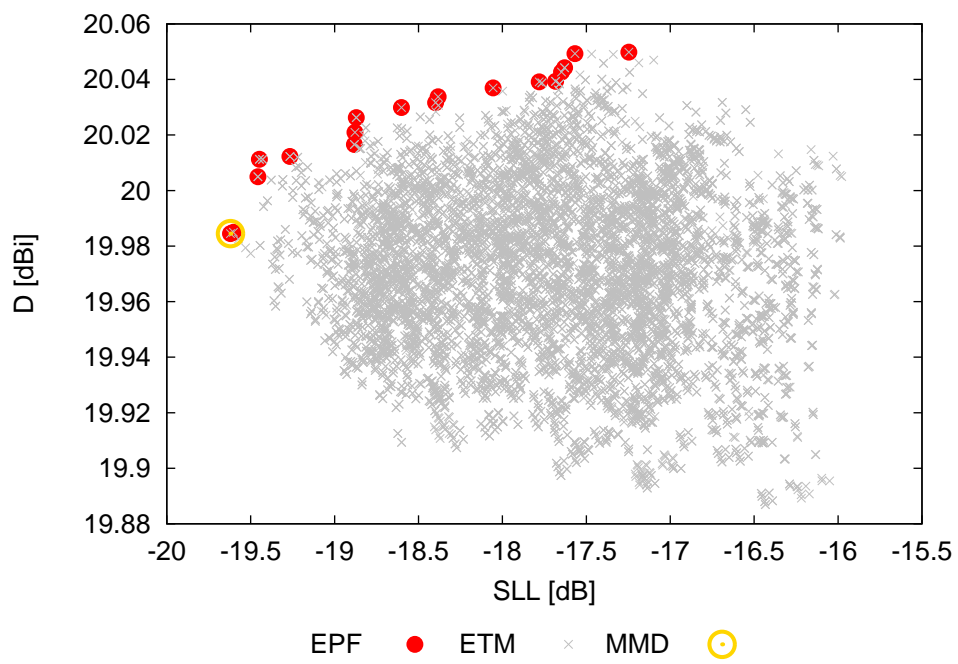
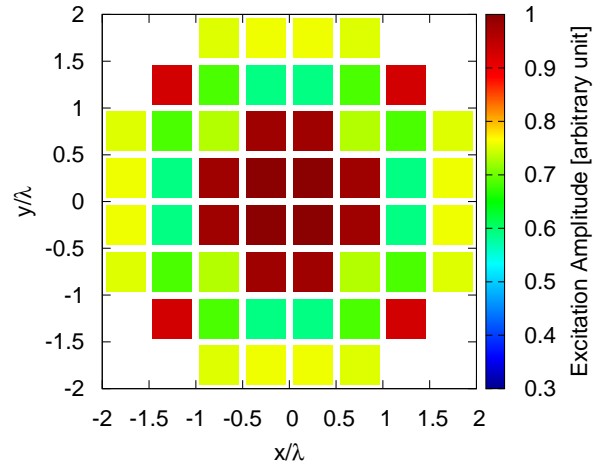
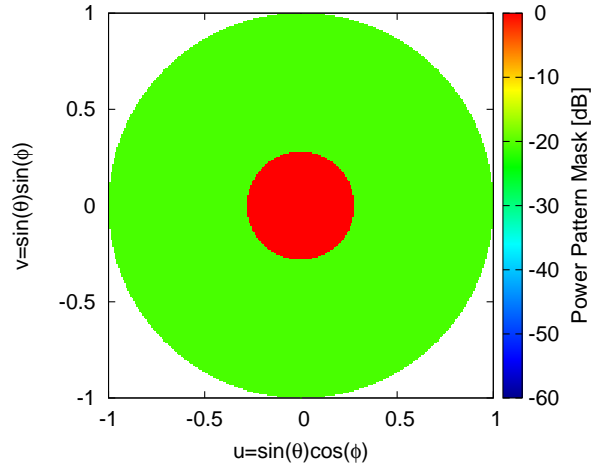


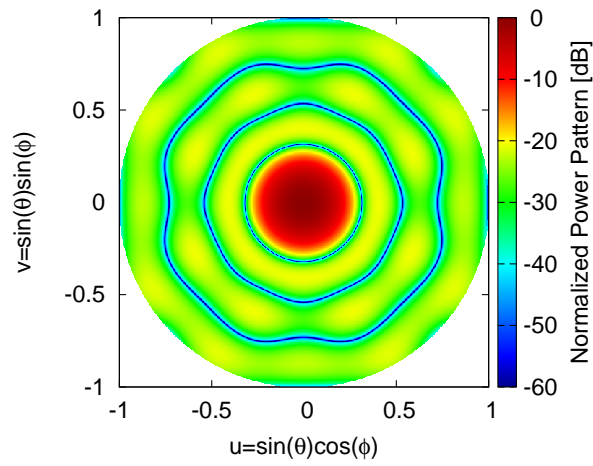
Fig. 7 - P. Rocca et al., “Pareto-Optimal Domino-Tiling of ...”



(a)



(b)



(c)

Fig. 8 - P. Rocca et al., “Pareto-Optimal Domino-Tiling of ...”

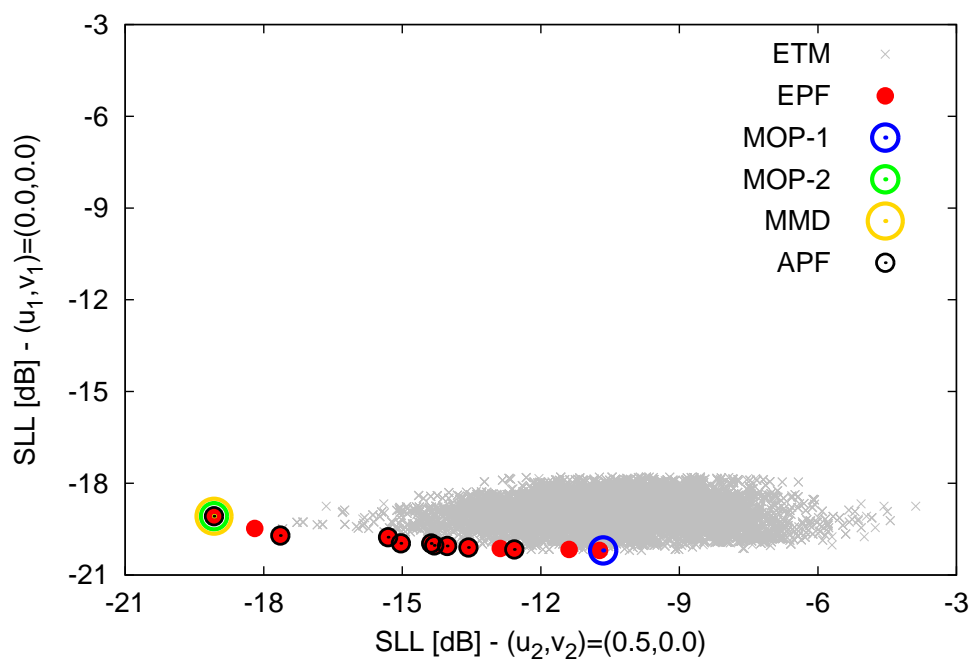
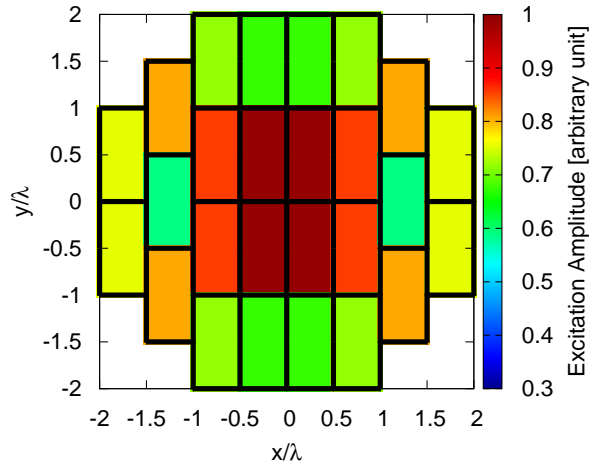
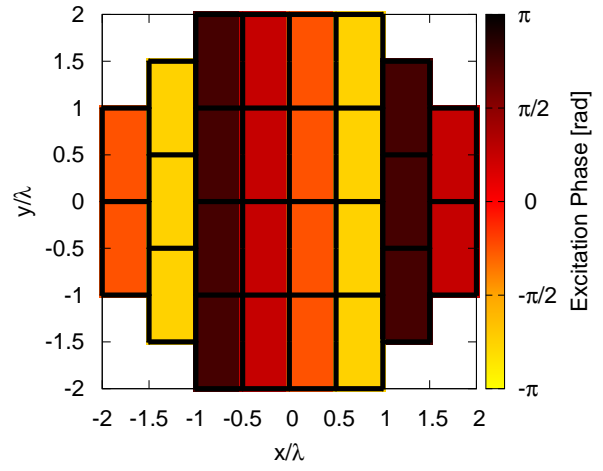


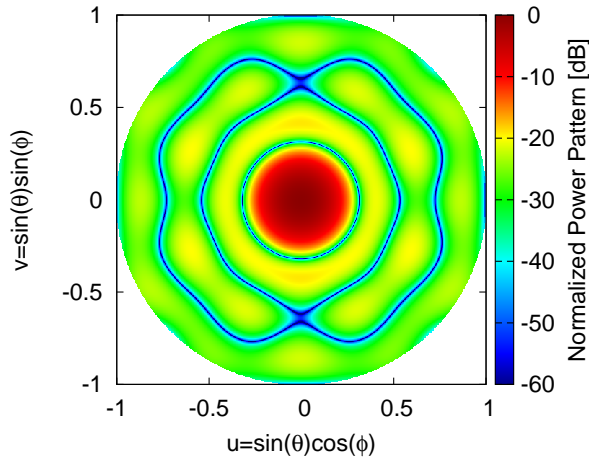
Fig. 9 - P. Rocca et *al.*, “Pareto-Optimal Domino-Tiling of ...”



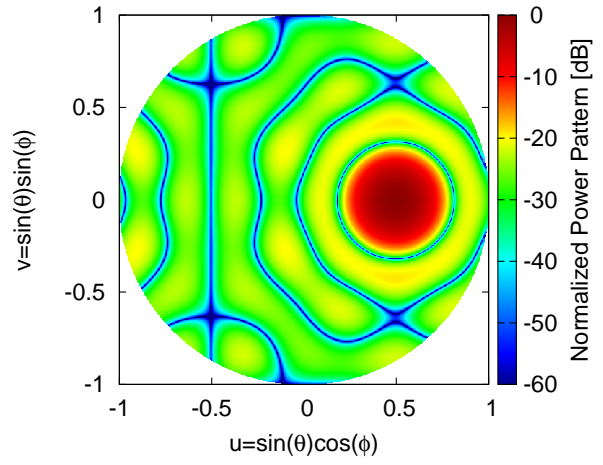
(a)



(b)



(c)



(d)

Fig. 10 - P. Rocca et al., “Pareto-Optimal Domino-Tiling of ...”

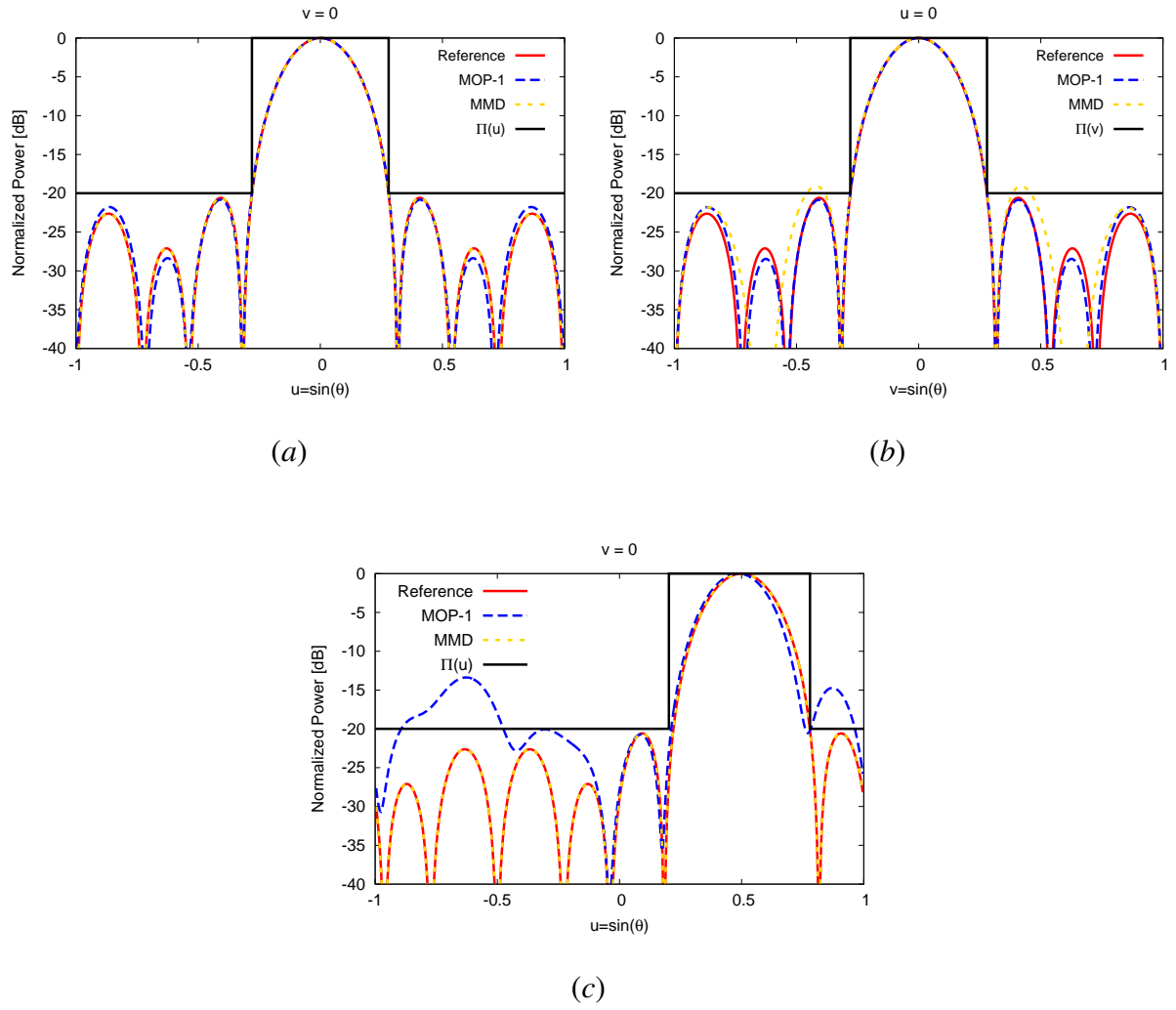
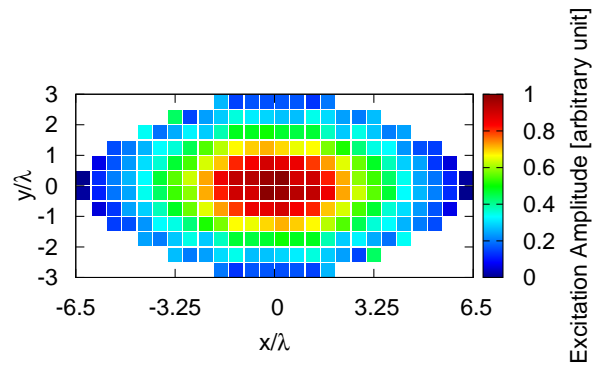
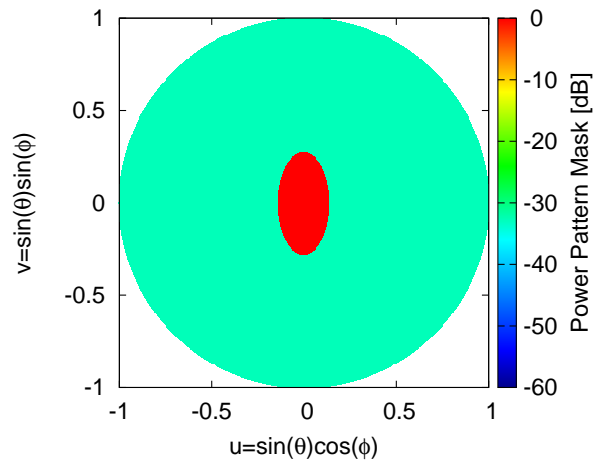


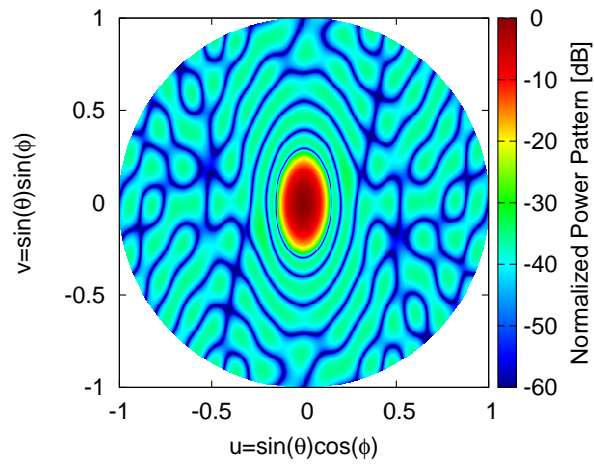
Fig. 11 - P. Rocca et al., “Pareto-Optimal Domino-Tiling of ...”



(a)



(b)



(c)

Fig. 12 - P. Rocca et al., “Pareto-Optimal Domino-Tiling of ...”

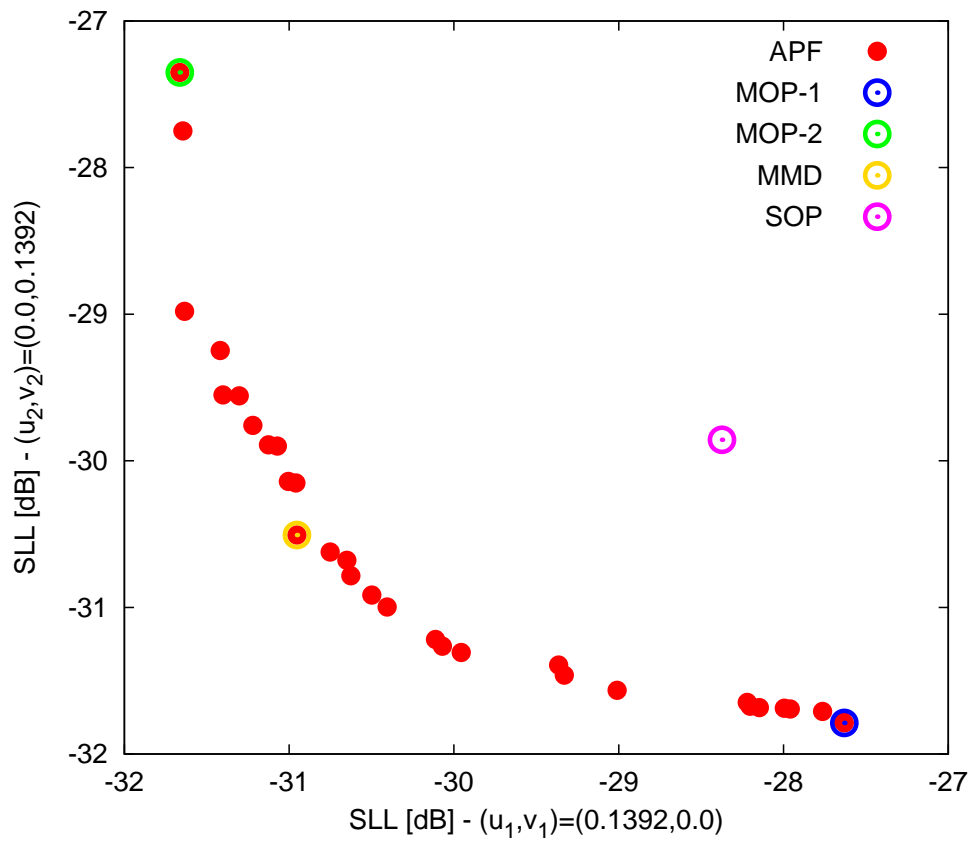


Fig. 13 - P. Rocca et al., “Pareto-Optimal Domino-Tiling of ...”

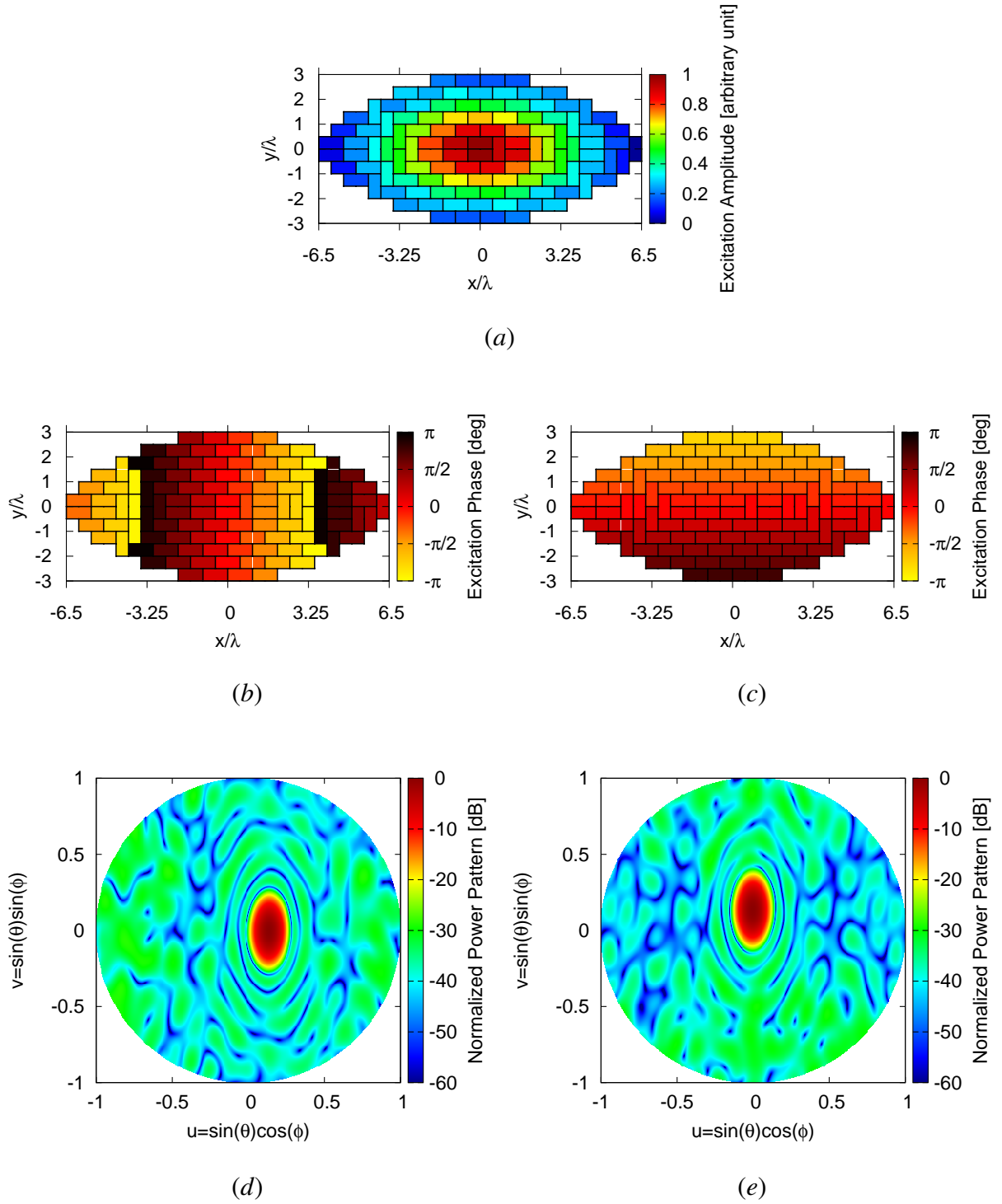


Fig. 14 - P. Rocca et al., “Pareto-Optimal Domino-Tiling of ...”

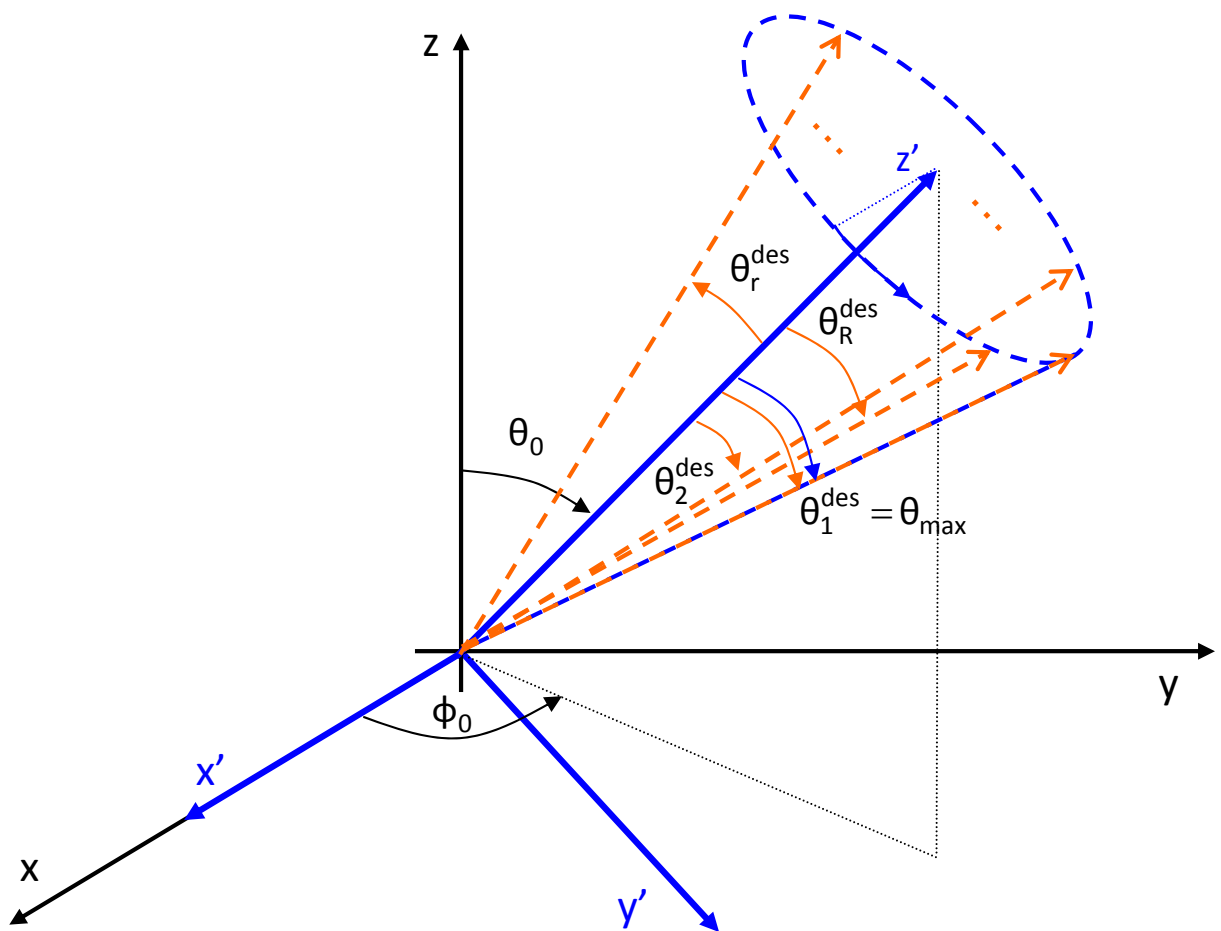


Fig. 15 - N. Anselmi *et al.*, “Orthogonal Polygon Array Design ...”

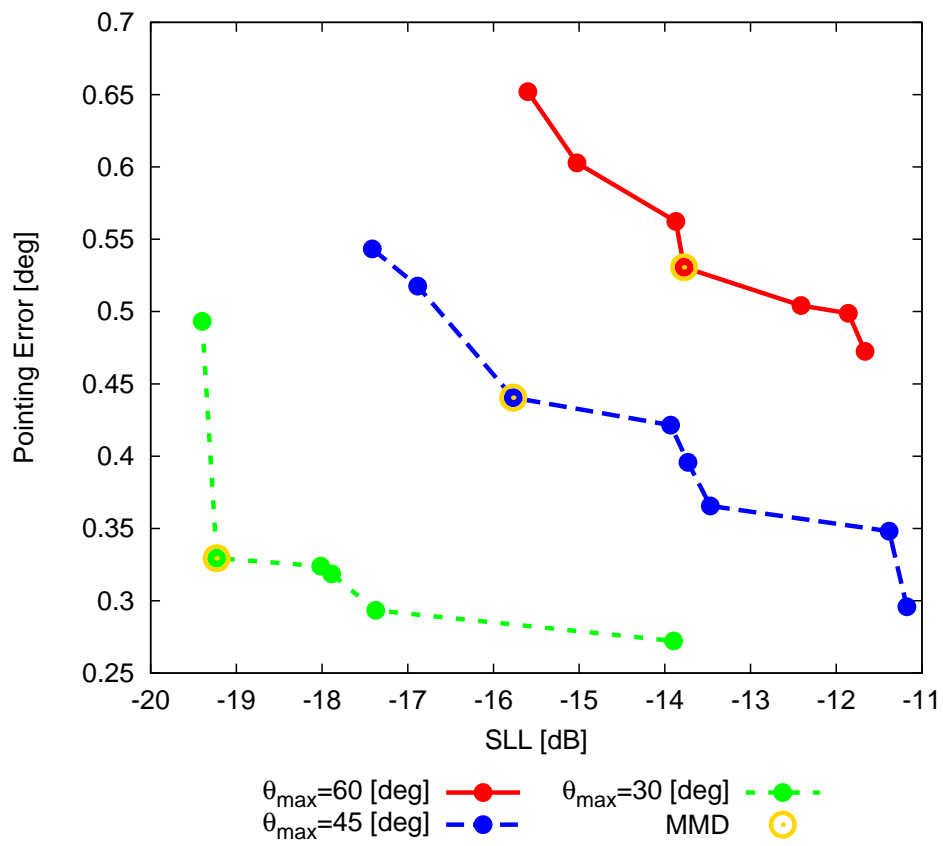
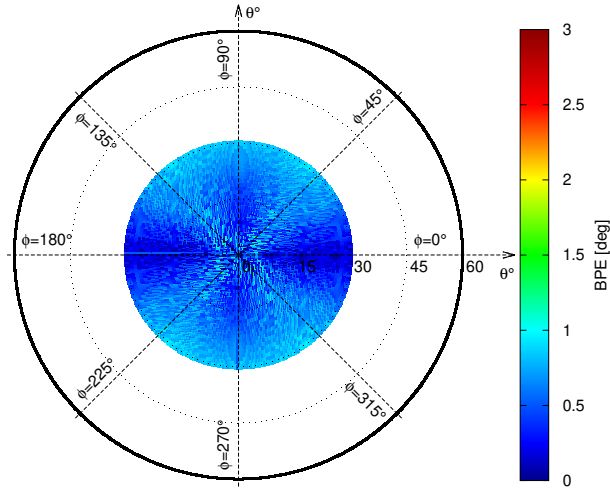
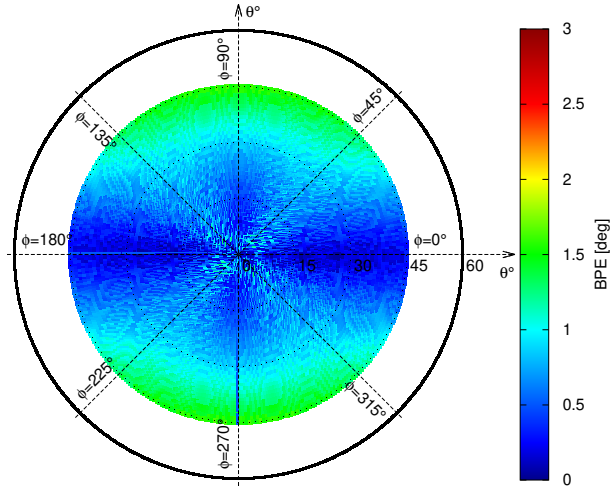


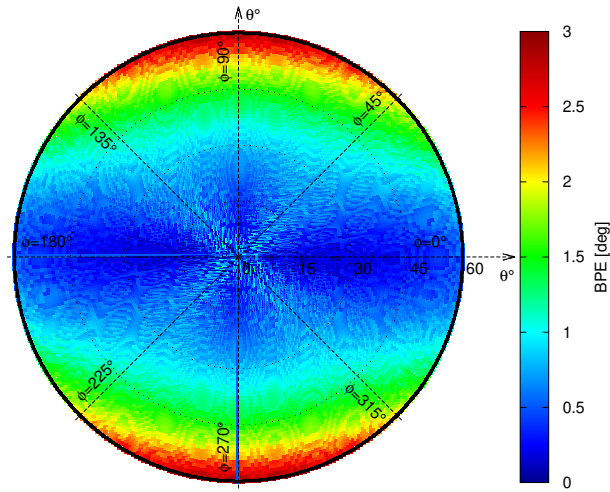
Fig. 16 - P. Rocca et al., “Pareto-Optimal Domino-Tiling of ...”



(a)



(b)



(c)

Fig. 18 - P. Rocca et al., "Pareto-Optimal Domino-Tiling of ..."

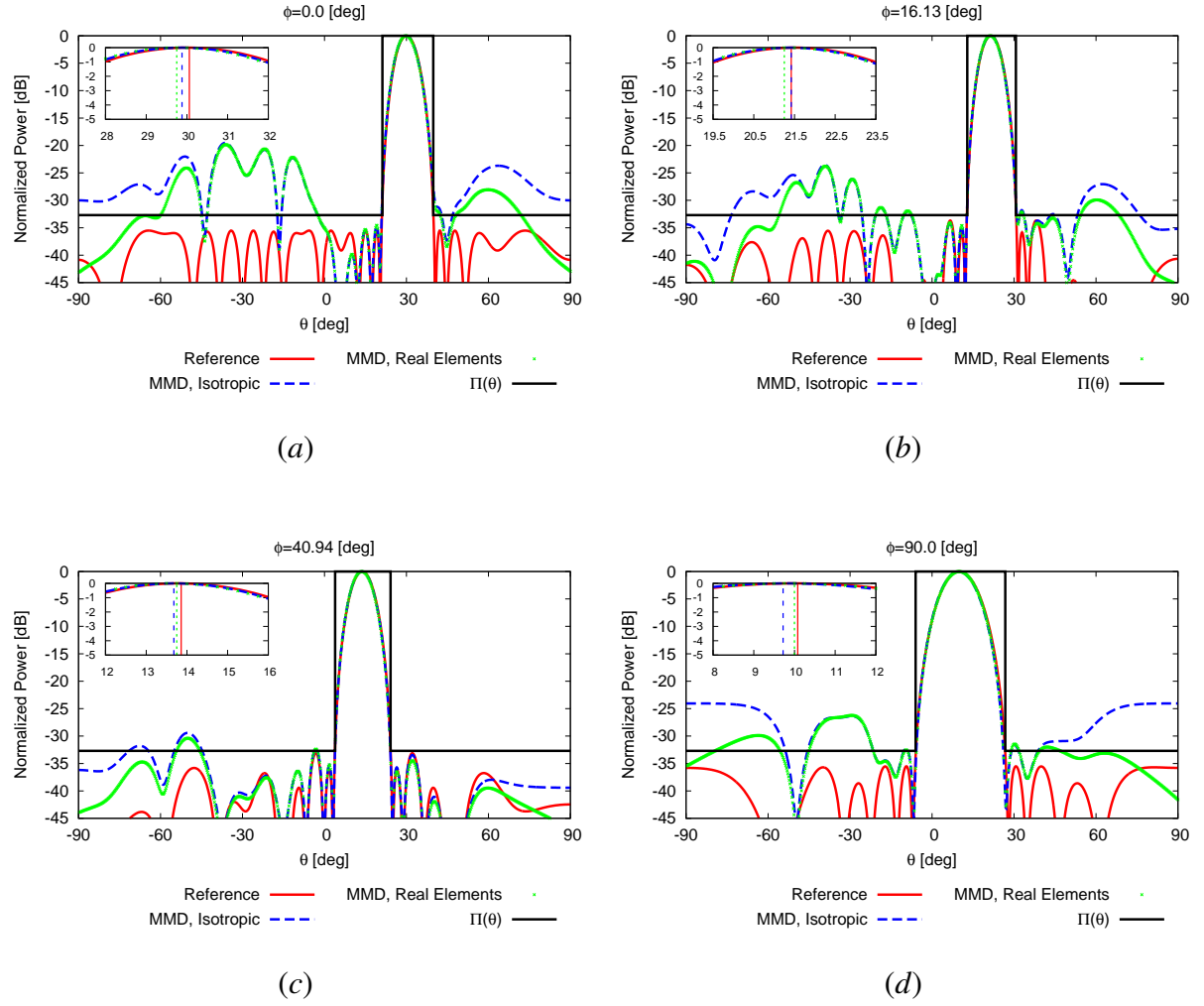


Fig. 18 - P. Rocca et al., “Pareto-Optimal Domino-Tiling of ...”

	SLL [dB]	D [dBi]	$HPBW_{az}$ [deg]	$HPBW_{el}$ [deg]
<i>Mask II</i>	-20.00	—	53.94	34.92
<i>Reference</i>	-20.00	19.94	21.12	15.62
<i>MMD</i>	-19.62	19.98	21.19	15.58

Tab. I - P. Rocca et al., “Pareto-Optimal Domino-Tiling of ...”

	SLL [dB]	D [dBi]	$HPBW_{az}$ [deg]	$HPBW_{el}$ [deg]
<i>Mask Π</i>	-20.00	—	32.52	32.53
	$(\theta_1, \phi_1) = (0, 0)$ [deg]			
<i>Reference</i>	-20.60	21.56	14.92	14.92
<i>MOP-1</i>	-20.16	21.57	14.96	14.96
<i>MOP-2</i>	-19.07	21.73	14.92	15.09
<i>MMD</i>	-19.07	21.73	14.92	15.09
	$(\theta_2, \phi_2) = (30, 0)$ [deg]			
<i>Reference</i>	-20.60	21.09	17.31	14.92
<i>MOP-1</i>	-10.65	19.59	16.54	15.85
<i>MOP-2</i>	-19.07	21.13	17.31	15.09
<i>MMD</i>	-19.07	21.13	17.31	15.09

Tab. II - P. Rocca et al., “Pareto-Optimal Domino-Tiling of ...”

	SLL [dB]	D [dBi]	$HPBW_{az}$ [deg]	$HPBW_{el}$ [deg]
<i>Mask</i> Π	-32.70	—	16.10	24.24
	$(\theta_1, \phi_1) = (8, 0)$ [deg]			
<i>Reference</i>	-32.70	27.15	6.11	12.03
<i>SOP</i>	-28.37	26.95	6.15	11.94
<i>MOP</i> - 1	-27.63	27.05	6.14	12.03
<i>MOP</i> - 2	-31.66	27.06	6.14	12.05
<i>MMD</i>	-30.97	27.03	6.14	12.04
	$(\theta_2, \phi_2) = (8, 90)$ [deg]			
<i>Reference</i>	-32.70	27.11	6.11	12.15
<i>SOP</i>	-29.86	27.05	6.10	12.04
<i>MOP</i> - 1	-31.79	27.11	6.11	12.13
<i>MOP</i> - 2	-27.35	27.07	6.10	12.11
<i>MMD</i>	-30.51	27.10	6.10	12.13

Tab. III - P. Rocca et al., “Pareto-Optimal Domino-Tiling of ...”

r	θ_r [deg]			ϕ_r [deg]
	$(\theta_{max} = 30)$	$(\theta_{max} = 45)$	$(\theta_{max} = 60)$	-
1	30.00	45.00	60.00	0.00
2	21.45	32.18	42.90	16.13
3	13.82	20.72	27.63	40.94
4	10.00	15.00	20.00	90.00
5	13.82	20.72	27.63	139.06
6	21.45	32.18	42.90	163.87
7	30.00	45.00	60.00	180.00
8	21.45	32.18	42.90	196.13
9	13.82	20.72	27.63	220.94
10	10.00	15.00	20.00	270.00
11	13.82	20.72	27.63	319.06
12	21.45	32.18	42.90	343.87

Tab. IV - P. Rocca et al., “Pareto-Optimal Domino-Tiling of ...”